I&EC research
Industrial & Engineering Chemistry Research

ARTICLE

pubs.acs.org/IECR

Transient Two-Dimensional Dehumidification and Desorption Behavior of Plate Desiccants under Humid Air Flow: a Conjugate Model That Includes Diffusion and Adsorption/Desorption within the Desiccant

Hassan S. Al-Sharqawi*

Department of Mechanical Technology, Medina College of Technology, P.O. Box 1593, Medina, Saudi Arabia

Noam Lior

Department of Mechanical Engineering and Applied Mechanics, University of Pennsylvania, Philadelphia, Pennsylvania 19104-6315, United States

ABSTRACT: A more rigorous conjugate-transient two-dimensional numerical model of solid bed desiccant systems (plates and narrow channels) used for gas dehumidification of a gas laminarly flowing along the desiccant, which, importantly, includes the associated transport through the desiccant body, was developed and validated. This improvement of the basic understanding of the process can be used for easier determination of ways for improving the overall performance of such systems. The solution provided a detailed exposition of the associated heat- and mass-transfer phenomena and of the desiccant performance, conducted here for both the adsorption and desorption processes in a range of air-flow Reynolds numbers and desiccant bed particle sizes and for two types of desiccant materials, silica gel and polystyrenesulfonic acid sodium salt (PSSASS) polymer. The results were also compared to those from an authors' simpler model that was published earlier and that does not consider transport through the solid desiccant. The new model was also employed to define and compute an "effective diffusion coefficient" from the basic composition of the desiccant, which is useful for characterizing desiccant properties and behavior in practical analysis. Besides the detailed behavior, some of the practical results are as follows: (i) the adsorption/desorption processes occur much faster at the flow entrance region; (ii) the mass-transport rates increase with the Reynolds number; (iii) within the studied range, manufacturing of the solid desiccant from larger particles raises its mass-transport rates; (iv) the water content and adsorption rate for PSSASS are larger than those for silica gel, thus making PSSASS a more effective desiccant than silica gel.

1. INTRODUCTION

The general objective of this study is to develop more rigorous models and an understanding of solid bed desiccant systems used for gas dehumidification, as well as to solve and analyze them specifically for desiccant-lined finite flat plates and channels. Significantly, and as an important advancement of the state of the art, the models we developed include flow-associated transport through the desiccant body. This improvement of the basic understanding of the process can be used for easier determination of ways for improving the overall performance of such systems. A conjugate-transient two-dimensional numerical solution for humid transient laminar air-flow fields over desiccant-lined finite flat plates composed of different desiccant particle sizes, and a detailed exposition of the associated heat- and mass-transfer phenomena and of the desiccant performance, is conducted here for both the absorption and desorption processes in a range of air-flow Reynolds numbers and desiccant bed particle sizes and for two types of desiccant materials.

One of the main initial past studies of a similar problem is that by the authors,[1] who developed and solved numerically a conjugate-transient two-dimensional flow and heat- and mass-transfer model of humid laminar air-flow fields over desiccant-lined finite flat plates. The solid desiccant model in their study was based on heat conduction and mass diffusion without including the flow-associated transport through the desiccant. Still using the same model, but in three dimensions, the authors later extended this study to the analysis of dehumidification in various desiccant duct geometries.[2]

The heat- and mass-transport model in the solid desiccant in the present study is advanced over those used by Al-Sharqawi and Lior[1,2] by posing and solving for the flow through the porous desiccant and the associated convective heat and mass transfer. This more detailed modeling should allow better insight into the desiccation and regeneration processes and also facilitate the discovery of better ways for their improvement.

The semiheuristic porous media equations by Vafai and Tien[3] are used to describe the flow and transport through the desiccant. This is an equivalent of the Navier−Stokes equation for such media and includes a version of the extended Darcy law for

Special Issue: Churchill Issue

Received: October 13, 2010
Accepted: February 16, 2011
Revised: February 13, 2011
Published: March 01, 2011

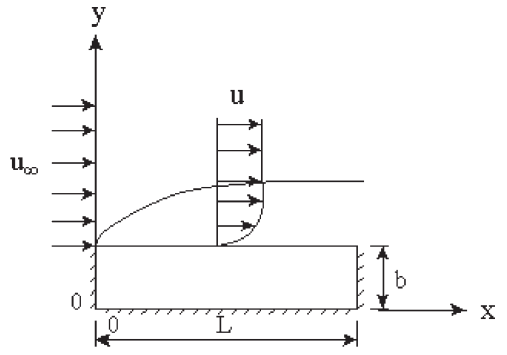

Figure 1. Physical configuration. A uniform velocity is applied at the leading edge.

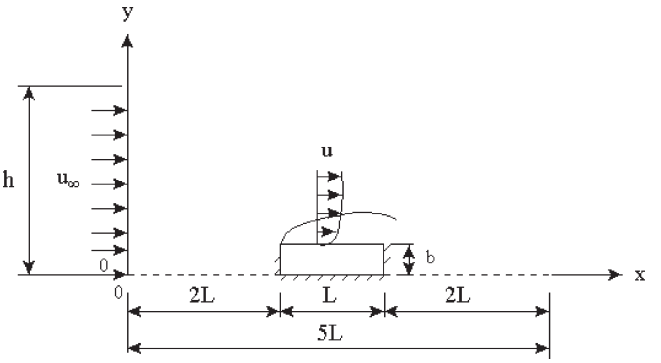

Figure 2. Extending the domain along the *x* direction.

conservation of momentum, where the microscopic viscous shear stress (Darcy term) and microscopic inertial forces (Ergun inertial term) are included.

As an example of a related use of this modeling approach and of its validation, we cite two past studies that have used it. Lee and Howell[4] computed the heat and mass transfer over and within a highly porous bed placed on the flat plate, at a location far upstream from the leading edge of the flat plate, for two-dimensional steady-state laminar flows. They used the semiheuristic Darcy momentum equation to describe the flow within the bed and the Navier–Stokes momentum equations to describe the flow outside it. They solved the energy equation numerically, to include and investigate the radiative transfer effects, and validated their numerical analysis experimentally. More recently, Betchen et al.[5] have developed a mathematical and numerical model for the treatment of conjugate fluid flow and the heat-transfer problem in a domain containing pure fluid, porous, and pure solid regions. They adopted a two-equation, local thermal nonequilibrium model in the porous region, solved the problem numerically using the finite-volume method, and validated their work by solving the Beavers–Joseph problem to depict the accuracy and utility of the conjugate formation. Also, they solved a porous plug flow for validation to depict the robustness of the interface condition and solved a documented heat-transfer problem to depict the utility of the nonequilibrium thermal model.

In this paper, the problem and model posed by Al-Sharqawi and Lior[1] (we name it "model 1"), but replacing the conductive/diffusive transport equations in the desiccant by the semiheuristic Darcy momentum, with heat- and mass-transfer equations, is posed and solved as a conjugate transient two-dimensional problem (we name it "model 2"). Different desiccant particle sizes as well as two types of desiccant materials, namely, silica gel and polymer desiccants, are considered. The results of this model 2 study are then compared with the results presented by Al-Sharqawi and Lior's[1] simpler model 1.

2. MODEL CONFIGURATION

The physical system considered (Figures 1 and 2) is a flat silica-gel-packed desiccant bed of length L with a uniform air stream passing over it in parallel. Figure 1 shows the extended computational domain of the flat bed along the x direction, where h is the practical height in the y direction, L is the bed length, and b is the bed thickness.

The extended domain up- and downstream of the bed was generated to allow the correct numerical solution of the flow field.

3. GOVERNING EQUATIONS

The geometry of model 2 is shown in Figure 2.

Region I: Air and Water Vapor

Continuity

$$\frac{\partial \rho_f}{\partial t} + \frac{\partial(\rho_f u_f)}{\partial x} + \frac{\partial(\rho_f v_f)}{\partial y} = 0 \tag{1}$$

x Momentum

$$\frac{\partial u_f}{\partial t} + u_f \frac{\partial u_f}{\partial x} + v_f \frac{\partial u}{\partial y} = -\frac{1}{\rho_f}\frac{\partial p}{\partial x} + \nu\left(\frac{\partial^2 u_f}{\partial x^2} + \frac{\partial^2 u_f}{\partial y^2}\right) \tag{2}$$

y Momentum

$$\frac{\partial v_f}{\partial t} + u_f \frac{\partial v_f}{\partial x} + v_f \frac{\partial v_f}{\partial y} = -\frac{1}{\rho_f}\frac{\partial p}{\partial y} + \nu\left(\frac{\partial^2 v_f}{\partial x^2} + \frac{\partial^2 v_f}{\partial y^2}\right) \tag{3}$$

Energy

$$\frac{\partial T_f}{\partial t} + u_f \frac{\partial T_f}{\partial x} + v_f \frac{\partial T_f}{\partial y} = \alpha_f\left(\frac{\partial^2 T_f}{\partial x^2} + \frac{\partial^2 T_f}{\partial y^2}\right) \tag{4}$$

Mass Diffusion (Water Vapor Diffusion in the Air Flow)

$$\frac{\partial C_f}{\partial t} + u_f \frac{\partial C_f}{\partial x} + v_f \frac{\partial C_f}{\partial y} = D_f\left(\frac{\partial^2 C_f}{\partial x^2} + \frac{\partial^2 C_f}{\partial y^2}\right) \tag{5}$$

Region II: The Silica Gel Bed

Continuity

$$\frac{\partial \rho_f}{\partial t} + \frac{\partial(\rho_f u_s)}{\partial x} + \frac{\partial(\rho_f v_s)}{\partial y} = 0 \tag{6}$$

Semiheuristic Darcy Momentum Equations[3]

x Momentum

$$\frac{\partial u_s}{\partial t} + u_s \frac{\partial u_s}{\partial x} + v_s \frac{\partial u_s}{\partial y} = -\frac{1}{\rho_f}\frac{\partial p}{\partial x} + \nu\left(\frac{\partial^2 u_s}{\partial x^2} + \frac{\partial^2 u_s}{\partial y^2}\right) - \frac{\nu\sigma}{K} u_s - \frac{C_E\sigma}{K^{1/2}} u_s{}^2 \tag{7}$$

dx.doi.org/10.1021/ie102086s |*Ind. Eng. Chem. Res.* 2011, 50, 8859–8880

y Momentum

$$\frac{\partial v_s}{\partial t} + u_s\frac{\partial v_s}{\partial x} + v_s\frac{\partial v_s}{\partial y} = -\frac{1}{\rho_f}\frac{\partial p}{\partial y} + \nu\left(\frac{\partial^2 v_s}{\partial x^2} + \frac{\partial^2 v_s}{\partial y^2}\right) - \frac{\nu\sigma}{K}v_s - \frac{C_E\sigma}{K^{1/2}}{v_s}^2 \quad (8)$$

where K is the permeability and C_E is the Ergun constant. The definition of the left-hand-side term in eqs 7 and 8 is the macroscopic inertial force. The definitions of the right-hand side terms in eqs 7 and 8 are as follows: (i) The first term is the forces acting on a fluid particle in terms of normal stress (the pore pressure gradient). (ii) The second term is the forces acting on a fluid particle in terms of macroscopic or bulk viscous shear-stress diffusion. (iii) The third term is the microscopic viscous shear stress, the Darcy term. (iv) The fourth term is the microscopic inertial force, also called the Ergun inertial term.[6]

For desiccant beds made of uniformly sized spherical particles of diameter d_p, the permeability K[7] is

$$K = \frac{\sigma^3}{180(1-\sigma)^2}{d_p}^2 \quad (9)$$

where d_p is the average particle diameter and σ is the desiccant bed porosity.

Deviations from the Darcy law for a macroscopic model are noticed when the Darcian velocity u_D is increased. These deviations are the result of the inertial contribution to the momentum balance. According to the Darcian velocity, the contributions of the viscous and inertial terms form the total resistance to the flow. However, for high velocity, according to Kaviany,[7] only the inertial contribution is relevant and dominates at very high velocities. Ergun[6] modified the Darcy law equation by accounting for the inertial (high-velocity) contribution. He also constructed a correlation that includes all of the fluid (velocity, viscosity, and density) and matrix parameters (closeness and orientation of the packing and size and shape of the particles). In his inertial term, the matrix parameters are combined and defined as

$$C_E = \frac{1.8(1-\sigma)}{\sigma^3}\frac{K^{1/2}}{d} \quad (10)$$

where C_E is the Ergun constant,[6,7] which is a porosity-, particle-diameter-, and permeability-dependent dimensionless constant.[8] The Ergun constant, C_E, is zero for low Reynolds number ($Re < 1$, pore level), where the Reynolds number for a pore is defined as

$$Re = \frac{\rho\bar{u}_p\bar{d}}{\mu} \quad (11)$$

where $\bar{u}_p$ is the average velocity in the pore and $\bar{d}$ is the average characteristic length scale for the pore. For large Reynolds numbers, the Ergun constant can be computed by eq 10.

Energy[6]

$$\rho_e c_e\frac{\partial T}{\partial t} + \rho_f c_f u_s\frac{\partial T_s}{\partial x} + \rho_f c_f v_s\frac{\partial T_s}{\partial y} = k_e\left(\frac{\partial^2 T_s}{\partial x^2} + \frac{\partial^2 T_s}{\partial y^2}\right) + H_l m''' \quad (12)$$

where H_l [kJ/kg] is the sorption heat, m''' [kg/s/m^3] is the water adsorption rate, $\rho_e c_e$ is the thermal capacity of the desiccant, ρ_f is the fluid density, c_f is the fluid specific heat, and k_e is the effective thermal conductivity.

$$\rho_e c_e = \sigma c_f\rho_f + (1-\sigma)\rho_s c_s \quad (13)$$

The effective thermal conductivity of desiccant beds made up of spherical particles with a parallel-pore model is (Table 3.1, p 130, Kaviany[7])

$$k_e = \sigma k_f + (1-\sigma)k_s \quad (14)$$

(in the parallel-pore model, it is assumed that the porous medium behaves like a set of alternate strata of fluid and solid, parallel to the mean heat flux[9]).

Water Vapor Diffusion[7]

$$\frac{\partial C_s}{\partial t} + u_s\frac{\partial C_s}{\partial x} + v_s\frac{\partial C_s}{\partial y} = D_f\left(\frac{\partial^2 C_s}{\partial x^2} + \frac{\partial^2 C_s}{\partial y^2}\right) - \frac{m'''}{\sigma\rho_f} \quad (15)$$

The water adsorption rate in the silica gel is expressed as

$$m''' = (1-\sigma)\rho_s\frac{\partial W}{\partial t} \quad (16)$$

The relationship between the water content in silica gel and the water vapor concentration at the local equilibrium, $W = f(C,T)$, is an empirical relationship, different for each desiccant. For silica gel[9,10] and the polystyrenesulfonic acid sodium salt (PSSASS) polymer,[11] the relationship used is

$$\phi = \frac{10^s C}{0.622 + C} \quad (17)$$

where

$$s = 4.21429 - \frac{7.5T_s}{237.3 + T_s} \quad (18)$$

for silica gel

$$(-\varphi - 9.31077 + 0.001717651T_s^2) + (478.0868 + 9.18715\times10^{-5}T_l^3)W - 1417.118W^2 + 2094.818W^3 = 0 \quad (19)$$

and for polymer (PSSASS)

$$(\varphi + 1.7649) - 110.0088W - 284.8653W^2 + 415.2553W^3 = 0 \quad (20)$$

where T_s is the silica gel temperature (°C) and T_1 is the ambient air temperature (°C).

In eqs 1−20, the unknown parameters in the air flow (region I) are u, v, T, and C and in the silica gel bed (region II) u, v, T, C, W, and m'''.

3.1. Interfacial Boundary Condition of a Porous Material. In model 1, the no-slip boundary condition was applied at the air−desiccant interface because the surface is considered impermeable and the heat conduction and mass diffusion in the desiccant were solved without including the convection term. In model 2, the no-slip boundary condition at the interface is no longer valid because the flow through the desiccant is taken into account and the surface is permeable, in which the external surface flow shear stress could create a tangential flow in the pores just below the surface,[12] which becomes more significant as the pore size increases. Beavers and Joseph[12] assumed that the

surface velocity u_f is a function of the mean tangential stress in the fluid outside the porous solid, expressed as an empirical slip boundary condition

$$\left(\frac{du}{dy}\right)_{y=0} = \frac{\alpha}{K^{1/2}}(u_f - u_s) \tag{21}$$

where α is the dimensionless slip parameter, K is the permeability, u_f is the slip velocity at the nominal surface, and u_s is the Darcy velocity inside the porous medium.

To calculate K and α for an idealized porous materiel, Richardson[13] investigated the flow formed above a corrugated surface by a plane surface moving parallel to the corrugations at a fixed distance from it. Taylor[14] demonstrated that α is independent of the geometry of the flow but depends only on the porous medium's properties by comparing his experimental results with Richardson's results. He showed that the slip coefficient α depends on the porosity σ and the structure of the porous medium, varying from 1 to 7. As the gap (pore) size increases in Taylor's model and the porosity tends to become 1.0, the limiting value of α reaches an asymptotic value of 1.308.

To apply the slip boundary condition appropriate to this study, we examine, using eq 21, the magnitude of the slip velocity Ω

$$\Omega = u_f - u_s = \frac{du}{dy}\frac{K^{1/2}}{\alpha} \tag{22}$$

If Ω is small enough compared with u_f, it is not necessary to assume slip. The magnitude of Ω is computed here (for $u_\infty = 0.1$ m/s, $Re_L = 333$, $T_\infty = 30$ °C, $C_\infty = 0.0276$ kg/kg, $C_b = 0.003\,775$ kg/kg, $W_0 = 0.08$ kg/kg, $b = 0.00321$ m, $x = 0.11$ m, and $t = 60$ s) for different particle diameters and at different locations along the bed length with bed porosity $\sigma = 0.5$ and $\alpha = 2.8$ found from ref 14, as shown in Tables 1 and 2. The value of α used here is for the corrugation surface and not for a complete packing bed because the latter's value is not reported in the literature.

The comparison between the magnitudes of u_f and Ω represented in Γ, the relative difference between Ω and u_f, for different x and particle diameters d_p, as shown in Tables 1 and 2, shows that the magnitude of Ω is small enough to consider it as zero, so we assume that $u_f = u_s$ and the no-slip condition are used.

Neale and Nader[15] suggested using the modified Darcy's law (Brinkman equation) including the viscous terms for the porous layer with the continuity of the velocity and shear stress to satisfy the no-slip condition. The continuity of the shear-stress condition at the interface indicates that the effects of viscous shear penetrate into the porous medium to form a boundary layer region, thus replacing the slip flow condition. This condition will be adopted in this analysis.

The momentum boundary condition at the air flow−desiccant interface is

$$\mu_f \frac{\partial u_f(2L < x < 3L,\ b,\ t)}{\partial y} = \mu_e \frac{\partial u_s(2L < x < 3L,\ b,\ t)}{\partial y} \tag{23}$$

$$\mu_f \frac{\partial v_f(2L < x < 3L,\ b,\ t)}{\partial y} = \mu_e \frac{\partial v_s(2L < x < 3L,\ b,\ t)}{\partial y} \tag{24}$$

where μ_f is the viscosity on the fluid side and μ_e is the effective viscosity in the solid desiccant bed and defined as

$$\mu_e = \sigma\mu_f + (1 - \sigma)\mu_s \tag{25}$$

Note that $\mu_s = 0$.

Table 1. Magnitude of the Absolute Slip Velocity Ω and Its Relative Effect Γ for Different Locations along the Bed Length with $d_p = 1.5 \times 10^{-3}$ m and $K = 0.71 \times 10^{-8}$

x, m	Ω, m/s	u_f, m/s	$\Gamma = (u_f - \Omega)/u_f \times 100$, %
0.11	8.5×10^{-4}	6.12×10^{-3}	86
0.125	6.34×10^{-4}	4.91×10^{-3}	88
0.14	5.4×10^{-4}	5.23×10^{-3}	90

Table 2. Magnitude of the Absolute Slip Velocity Ω and Its Relative Effect Γ for Different Particle Diameters at $x = 0.125$ m

	permeability			$\Gamma = (u_f - \Omega)/$
d_p, m	K	Ω, m/s	u_f, m/s	$u_f \times 100$, %
1.5×10^{-3}	0.71×10^{-8}	6.34×10^{-4}	4.91×10^{-3}	87
1×10^{-3}	2.78×10^{-9}	2.45×10^{-4}	4.367×10^{-3}	94
0.1×10^{-3}	2.78×10^{-11}	2.4×10^{-5}	4.196×10^{-3}	94

3.2. Boundary Conditions. The boundary conditions here are the same as those presented in ref 1 except for the following conditions:

Interfacial Energy−Mass Balance at the Air Flow−Desiccant Interface

$$-k_s\frac{\partial T}{\partial y} + h_s\rho_s\left(C_1 v - D_{12}\frac{\partial C_1}{\partial y}\right)_s = -k_f\frac{\partial T}{\partial y} + (h_1 - h_2)\rho_f\left(C_1 v - D_{12}\frac{\partial C_1}{\partial y}\right)_f + h_2\rho_f v\Big|_f \tag{26}$$

The enthalpy in the solid desiccant, h_s, is defined as

$$h_s = H_l + c_{pv}T \tag{27}$$

where H_l is the heat of sorption.

The enthalpy of the water vapor h_1 is defined as

$$h_1 = h_g + c_{pv}T \tag{28}$$

where h_g is the enthalpy of saturated water vapor and is equal to 2501.3 kJ/kg at 0 °C.

The enthalpy of the air h_2 is defined as

$$h_2 = c_{pa}T \tag{29}$$

The specific heat of the water vapor and air are $c_{pv} = 1.86$ kJ/kg·K and $c_{pa} = 1.01$ kJ/kg·K, respectively.[18] They are assumed to be constant because their variations with temperature in our temperature range of interest are very small. For example, in our study, the temperature changes by about 4 °C, with a corresponding air specific heat change of only about 0.4%.

No heat or mass flux in the silica gel bed in the x direction at $x = 2L$ (the left edge of the bed)

$$\frac{\partial T_s(2L,\ y \le b,\ t)}{\partial x} = \frac{\partial C_s(2L,\ y \le b,\ t)}{\partial x} = 0 \tag{30}$$

No flow through the left edge of the bed, at $x = 2L$

$$u_s(2L,\ y \le b,\ t) = v_s(2L,\ y \le b,\ t) = 0 \tag{31}$$

dx.doi.org/10.1021/ie102086s |Ind. Eng. Chem. Res. 2011, 50, 8859–8880

No heat or mass flux in the x direction at $x = 3L$ (the right edge of the bed)

$$\frac{\partial T_s(3L,\ y \le b,\ t)}{\partial x} = \frac{\partial C_s(3L,\ y \le b,\ t)}{\partial x} = 0 \qquad (32)$$

No flow through the right edge of the bed, at $x = 3L$

$$u_s(3L,\ y \le b,\ t) = v_s(3L,\ y \le b,\ t) = 0 \qquad (33)$$

No flow through the bed bottom

$$u(2L < x < 3L,\ 0,\ t) = v(2L < x < 3L,\ 0,\ t) = 0 \qquad (34)$$

3.3. Initial Conditions

$$u_f(x, y, 0) = u_\infty \qquad (35)$$

$$T_f(x, y, 0) = T_\infty \qquad (36)$$

$$C_f(x, y, 0) = C_\infty \qquad (37)$$

$$C_s(2L < x < 3L,\ y \le b,\ 0) = C_0 \qquad (38)$$

$$W(2L < x < 3L,\ y \le b,\ 0) = f(C_0, T_\infty) \qquad (39)$$

3.4. Computational Parameter Values. The choice of the specific variables in the analysis was based on practical values in desiccant systems and on the numerical modeling consideration. For the former, the air-flow velocity and associated Reynolds number vary significantly depending on the system configuration and channel dimensions and are typically between somewhat less than 0.1 m/s and up to somewhat more than 2 m/s. While higher velocities improve transport, they increase the pressure drop, and thus energy consumption and system cost, and require longer desiccant passages, which increase the price and bulk of the system. The latter, numerical modeling/simulation considerations, favor a smaller geometry and lower Reynolds numbers. As to the desiccant bed thickness, those too vary widely in practice, but about $^1/_8$ in. or 3 mm is a reasonable value. The parameter values that were thus chosen for the computation are sort of an optimum between practical and numerical considerations: 0.1 m/s $\le u_\infty \le$ 0.5 m/s ($333 \le Re_L \le 1667$), T_∞ = 30 °C, C_∞ = 0.0276 kg/kg, C_b = 0.003 775 kg/kg, W_0 = 0.08 kg/kg, b = 0.00321 m, L = 0.05 m, and t = 20 s.

The values of the initial concentration in the air and desiccant bed regions were selected using the psychrometric chart based on the consideration of the air region to be very humid (RH 85%) and the solid desiccant to be almost dry (RH 15%) at T_∞ = 30 °C. The value of the water content W_0 was computed by eqs 16−20.

4. DESICCANT BED PROPERTIES

4.1. Permeability. The meaning and derivation of the permeability K, used in eq 9, are presented by Kaviany.[7]

The range of K for different spherical particle diameters d_p used in this chapter is shown in Table 3.

For a circular capillary cross section, k_0 = 2.0, the permeability is 25% larger than that of the noncircular capillary cross section, where k_0 = 2.5 (rectangular, elliptical, and annular shapes).

Lee and Howell[7] calculated the permeability K for four different ceramic foam samples in their study. The range of K was between 1.42×10^{-7} and 7.67×10^{-7} m^2.

4.2. Relationship between the Desiccant Bed Porosity, Packing, and Particle Size. When the desiccant bed is packed with uniform spheres, there are two types of packing: regular (ordered) and irregular (random). In regular packing, the particles are arranged in a regular array. In irregular (random) packing, the particles are formed by the haphazard positioning of particles to form the desiccant bed. The porosities of these two types of packing are independent of the particle's diameters as reported by Reyes and Iglesia[19] in their analysis. The porosity of regularly packed beds of uniform spherical particles is 0.48,[20] and that of randomly packed beds 0.42.[19] In this study, it is assumed that the desiccant bed is regularly packed because its porosity is close to the randomly packed one anyway: in our first study,[21] the conjugate heat- and mass-transfer problem in the desiccant bed was solved with different porosities and the overall water contents in the desiccant bed with 0.48 and 0.42 porosities were 0.122 and 0.119 kg/kg, respectively, different by just 2.5%.

The porosity of beds composed of nonuniform size particles according to Reyes and Iglesia[19] is 10% lower than those made of uniform spheres, for which the porosity is 0.37. Ouchiyama and Tanaka[22] also reported similar results.

5. NUMERICAL METHOD AND ERROR ANALYSIS

The continuity and momentum equations were solved by the *SIMPLER* (Semi-Implicit Method for Pressure-Linked Equation Revised) algorithm control-volume method.[23] The numerical method was validated here by checking the grid dependence and convergence. Both the average and maximal relative errors in the computed u velocity as a function of the grid size were computed as a function of the grid size and plotted. The average relative error is defined as

$$E_{r,\,ave,\,big} = \frac{1}{ij}\sum_{i,j}\frac{u_{big}(i,j) - u_{small}(i,j)}{u_{big}(i,j)} \qquad (40)$$

where $u_{big}(i,j)$ and $u_{small}(i,j)$ are the u velocities of the big and small grid sizes in the x and y directions, respectively, and i and j are the grid point numbers in the x and y directions. The maximum relative error ($E_{r,max}$) is the maximum among the relative errors in the computational domain. Both errors are seen to decrease as the grid size (spacing) decreases in an asymptotic way, proving grid independence at a grid of 250 points in the x direction and 150 points in the y direction. The computational error at that grid, which was used in the computations in this paper, was 1×10^{-4}. The convergence of E_r was also analyzed and proven. About 46 iterations are needed for convergence, and the number of iterations used is 120−250, depending on the case being solved.

Table 3. Bed Permeability K versus Particle Diameter d_p

	permeability K for	
particle diameter d_p, m	k_0 = 2.0	k_0 = 2.5
1.5×10^{-3}	0.89×10^{-8}	0.71×10^{-8}
1×10^{-3}	3.472×10^{-9}	2.78×10^{-9}
0.1×10^{-3}	3.472×10^{-11}	2.78×10^{-11}

Parts a and b of Figure 3 show the average and maximum relative errors in the computed velocity u as a function of the grid size for both the entire domain of model 2 and the desiccant domain in model 2, respectively. It is seen that the average and maximum relative errors decrease asymptotically as the grid size decreases, proving convergence. The average relative errors in the desiccant bed domain in Figure 3b at $\Delta x/L = 0.024$ and 0.0112 are 50% and 16%, respectively, larger than those for the entire domain (Figure 3a).

Figure 4 shows the magnitudes of the computed u velocities at the desiccant surface and inside the desiccant bed as a function of the grid size, extrapolated to zero grid size (at point 5). The conditions of this run are $u_\infty = 0.1$ m/s, $Re_L = 333$, $T_\infty = 30$ °C, $C_\infty = 0.0276$ kg/kg, $C_b = 0.003\,775$ kg/kg, $W_0 = 0.08$ kg/kg, $b = 3.21$ mm, $x = 0.11$ m, $t = 60$ s, $d_p = 1.5 \times 10^{-3}$ m, and $K = 0.711 \times 10^{-8}$. The extrapolation was made by performing curve fitting using a quadratic polynomial equation, aiming to have the curve approach $x = 0$ at an angle normal to the ordinate and thus establishing point 5 there. The magnitudes of the u velocities at point 5 on the surface and inside the bed are 11% and 6%, respectively, smaller than the magnitudes of the u velocity at point 2, which indicates that the u values that we compute inside the desiccant are meaningful.

Similarly, Figure 5 shows the magnitudes of the v velocities at the desiccant surface and inside the desiccant bed as a function of the grid size. It also shows the absolute error. The magnitudes of the v velocities at point 5 on the surface and inside the bed are 13% and 11%, respectively, smaller than the magnitudes of the v velocities at point 2, which indicates that the v values that we compute inside the desiccant are meaningful.

6. RESULTS AND DISCUSSION

In this section, the validation and results of model 2 are presented and discussed. This model is the same as the problem and model posed by Al-Sharqawi and Lior[1] (we name it model 1), but replacing the conductive/diffusive transport equations in the desiccant by the semiheuristic Darcy momentum, with heat- and mass-transfer equations, is posed and solved as a conjugate transient two-dimensional problem (we name it model 2). Different desiccant particle sizes as well as two types of desiccant materials, namely, silica gel and polymer desiccants, are considered. The results of this model 2 study are then compared with the results presented by Al-Sharqawi and Lior's[1] simpler model 1.

6.1. Validation. Because we did not perform experiments on this topic, we have found some published experiments and analyses by others and ran our model for their conditions to compare the results. Such a method of validation naturally suffers from incomplete knowledge of all conditions employed by these researchers, some differences between the geometric configurations, and a lack of clear knowledge of the accuracy of their results, but it does increase confidence in our results if they are at least reasonably close. We note that they used the naphthalene sublimation technique in their experiments, instead of direct heat and mass transfer, and that their experiment deployed the porous plate on top of the naphthalene one, creating a somewhat different geometry and a different flow pattern than those in our case, especially different upstream and downstream vortices and wakes, which affect the mass and heat transport, and it is therefore hard to assess the error. The input parameters that Lee and Howell[4] used for sample IV (the closest in permeability K to our case, from their Table 1 and Figure 10) in their experimental and theoretical studies were used in our model 2 for one of the comparisons. They found the Sherwood number experimentally, and they used it to validate their numerical results. The Sherwood number is defined as

$$Sh = \frac{h_m b}{D_f} \tag{41}$$

where h_m is the convective mass-transfer coefficient, b is the desiccant bed thickness, and D_f is the diffusion coefficient.

The conditions of Lee and Howell's analysis[4] (their Figure 10) used in this comparison are $Re = 4500$, $\sigma = 0.83$, $K = 1.4 \times 10^{-7}$, and $b = 0.011$ m. Figure 6 shows that while the numerical and experimental results of ref 4 are only in qualitative agreement with each other for the smallest values of K examined in ref 4, their numerical results agree within 10−50% with our model 2 predictions of the Sherwood number as a function of x. As to the large difference between their own experimental and numerical results, they are shown in ref 4 to be in reasonable agreement with each other for larger values of the permeability K but not for the smallest permeability that they studied, and that is shown in our Figure 6, which is much closer to the permeabilities of the porous medium in our study.

Another validation that we performed was to use the results of the heat and mass transport for model 2 to compare Pesaran and Mills' theoretical model and experimental[24,25] results. The comparison is shown in ref 21 (Figure 4.13a,b), which demonstrates that the outlet temperature and concentration as a function of time computed by model 2 are in close agreement with Pesaran and Mills' results, within 2.5 °C for the temperature and 12% for the concentration.

6.2. Flow-Field Results. *6.2.1. Reduction of Velocity Overshoots.* An interesting phenomenon was encountered during the flow computations over a finite length plate modeled as shown in Figure 1: when the uniform free stream velocity was applied at the leading edge, the results have shown a 12% velocity overshoot (over the free stream velocity) near the boundary layer edge. Such overshoots in flows over plates were measured[26] in laminar flow ($20 < Re < 3000$), and computationally predicted by others[27] for $10^2 < Re < 10^5$, at the trailing edge and the near wake but not over the plate, as our initial results have shown. Several different approaches were undertaken by us, as explained in detail inrefs 1 and 21 to examine whether this velocity overshoot is just a computational artifact as it seemed to be, and several methods, including grid refinement and extension of the computational domain further in the y direction to allow a more gradual approach to the boundary conditions at the top of the domain, were used, but it remained there. While the overshoot was seen to decrease by extension of the computational domain by a length $2L$ both upstream and downstream of the plate along the x direction, further changes in the computational method show that it exists and is likely to be a real physical phenomenon. We also found that the overshoot decreases somewhat as the Reynolds number (Re_L) increases, even without having to extend the computational domain along x, falling below about 3% for $Re \sim 27\,000$ ($u_\infty = 8$ m/s).

6.2.2. Velocity Field. We start with a somewhat detailed description of the computed flow field because the flow inside and outside the desiccant bed obviously has a significant impact on heat and mass transfer and the desiccant performance in general and is especially interesting in this model that allows its prediction inside the bed.

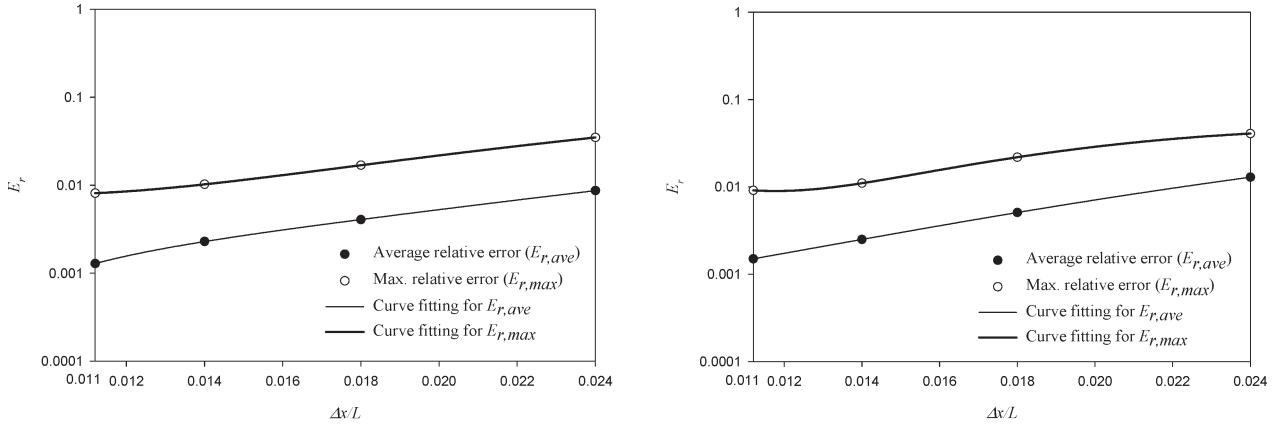

a. In the entire domain **b.** In the desiccant bed

Figure 3. Relative error in the computed u velocity for model 2 (a) in the entire domain and (b) in the desiccant bed as a function of the grid size.

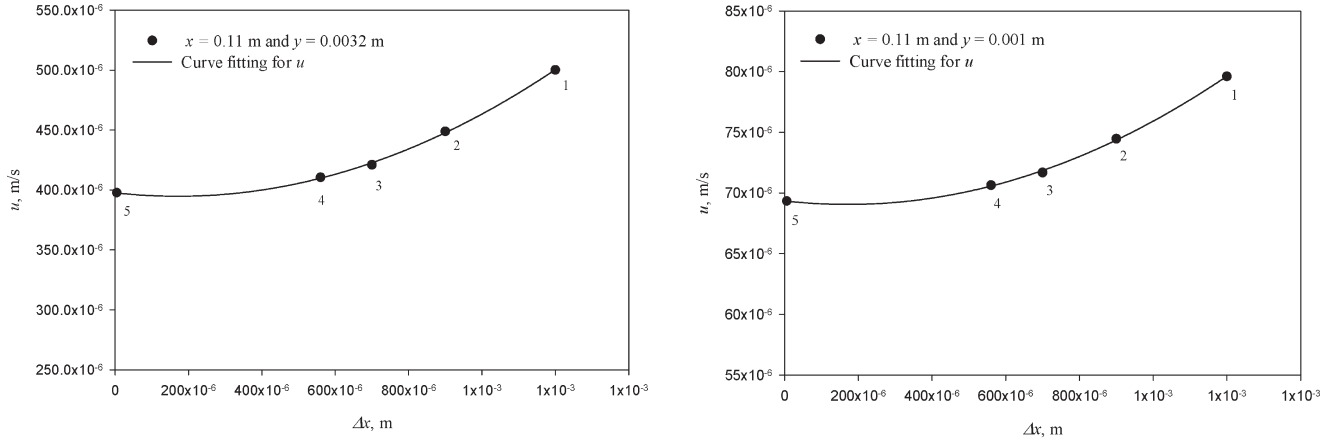

a. At surface **b.** Inside bed

Figure 4. u velocity in the desiccant bed and on its surface, computed for grid sizes denoted by numbers 1−4 and extrapolated to $\Delta x = 0$, point 5.

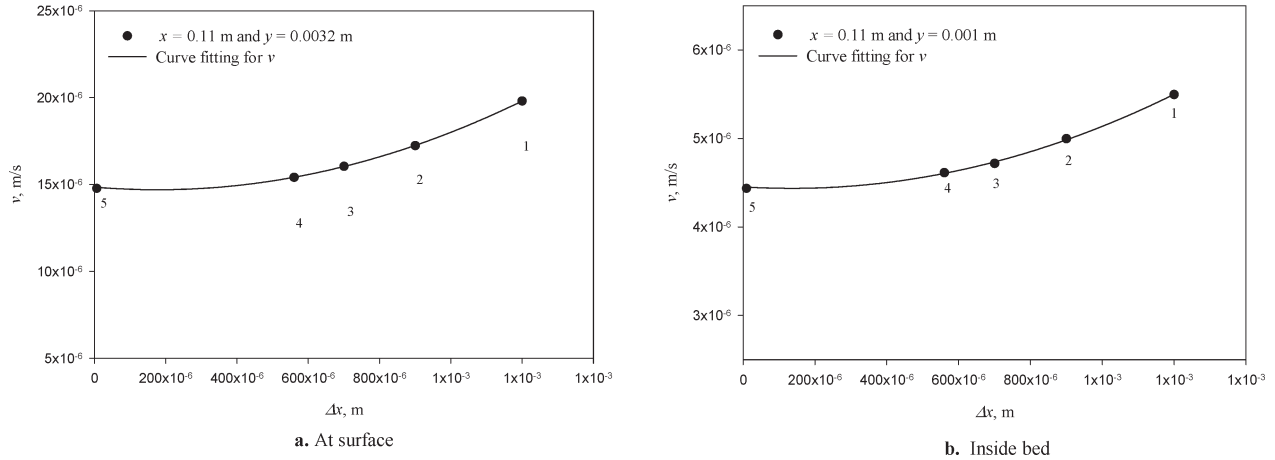

a. At surface **b.** Inside bed

Figure 5. v velocity in the desiccant bed, computed for grid sizes denoted by numbers 1−4 and extrapolated to $\Delta x = 0$, point 5.

Figures 7 and 8 show the u and v velocity profiles at the same t = 60 s over and within the silica gel bed of spherical particles $d_p = 1.5 \times 10^{-3}$ m, at different x. Because the velocity field over and within the polymer bed is mostly the same as that of the silica gel bed, we present in this section only the velocity results of the silica gel bed. The boundary layer is built up along the bed as shown in Figure 7a.

dx.doi.org/10.1021/ie102086s |*Ind. Eng. Chem. Res.* 2011, 50, 8859–8880

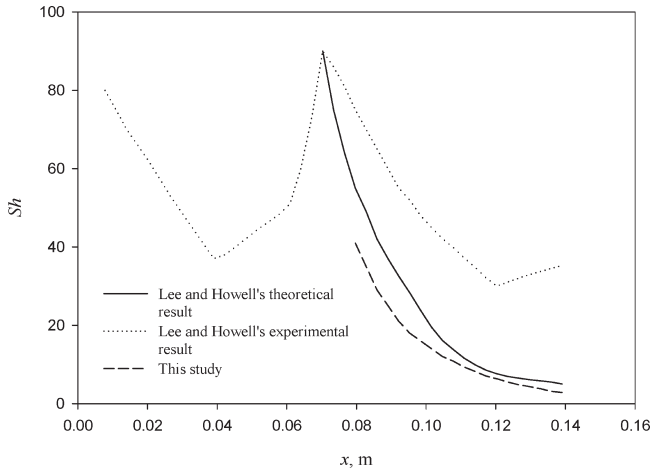

Figure 6. Comparison of the Sherwood number as a function of x for this study and Lee and Howell's theoretical and experimental model.[4] Re = 4500, σ = 0.84, $K = 1.4 \times 10^{-7}$, and b = 0.011 m.

The magnitude of u inside the desiccant bed decreases in the downward direction because of the no-slip boundary condition at the bottom surface in which the boundary layer is formed inside the bed due to the effect of the viscous shear stress caused by the continuity shear-stress boundary condition at the flow—desiccant interface, as shown in Figure 7b. This figure also depicts the direction of u, which becomes negative at y = 0.0025 m and toward the bottom. The backflow is due to the increase in the pressure inside the bed imposed by the outside flow near the step leading edge of the bed.

The magnitudes of the u velocities at the bed surface (y = 0.0032 m) and inside the bed (y = 0.0015 m) are lower by about 0.13% and 75%, respectively, as x changes from 0.1 to 0.125 m due to an increase in the pressure at the surface along the bed length, as shown in Figure 7b. The magnitudes of the v velocities at the bed surface (y = 0.0032 m) and inside the bed (y = 0.0015 m) are lower by about 54% and 29%, respectively, as x changes from 0.1 to 0.125 m due to an increase in the pressure at the surface along the bed length, as shown in Figure 8b. As expected, the v velocity inside the desiccant bed is in the negative direction

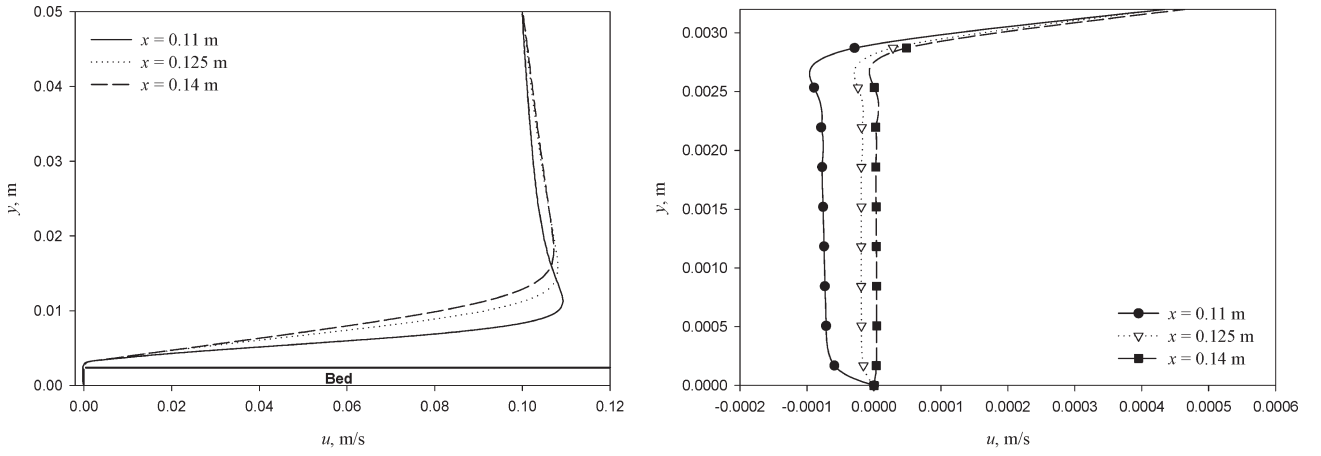

a. Over the bed **b.** Within the bed

Figure 7. u velocity profiles over and within the silica gel bed for model 2 as a function of y at different x. u_∞ = 0.1 m/s, Re_L = 333, T_∞ = 30 °C, C_∞ = 0.0276 kg/kg, C_b = 0.003 775 kg/kg, W_0 = 0.08 kg/kg, b = 0.00321 m, L = 0.05 m, h = 0.05 m, t = 60 s, $d_p = 1.5 \times 10^{-3}$ m, and $K = 0.71 \times 10^{-8}$.

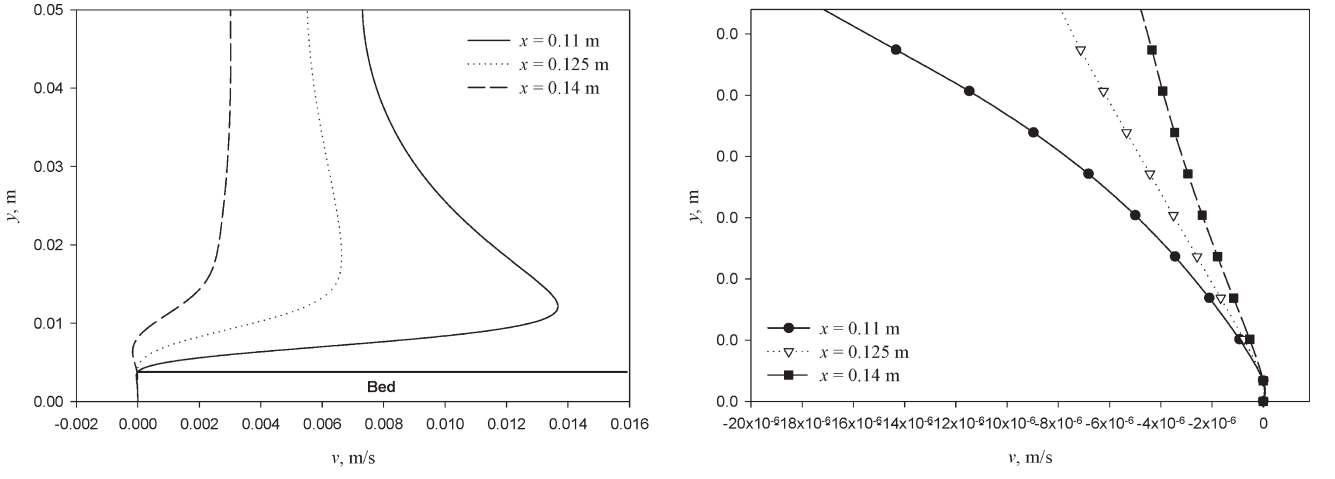

a. Over the bed **b.** Within the bed

Figure 8. v velocity profiles over and within the silica gel bed for model 2 as a function of y at different x. u_∞ = 0.1 m/s, Re_L = 333, T_∞ = 30 °C, C_∞ = 0.0276 kg/kg, C_b = 0.003 775 kg/kg, W_0 = 0.08 kg/kg, b = 0.00321 m, L = 0.05 m, h = 0.05 m, t = 60 s, $d_p = 1.5 \times 10^{-3}$ m, and $K = 0.71 \times 10^{-8}$.

dx.doi.org/10.1021/ie102086s |Ind. Eng. Chem. Res. 2011, 50, 8859–8880

(into the desiccant) because of the water vapor adsorption by the desiccant and the flow-induced suction. The u velocity inside the bed is positive starting from the leading edge up to $x = 0.105$ m, and then it changes to negative, which means that backflow occurs.

Figures 9 and 10 show the effect of the particle diameter on the u and v profiles above and inside the desiccant bed for both models 1 and 2. The magnitudes of u and v are not affected by changing the permeability over the bed, as shown in Figures 9a and 10a. Inside the bed, however, the magnitudes of the u and v velocities decrease as d_p decreases. The magnitudes of u and v at the bed surface ($y = 0.0032$ m) for particle diameter $d_p = 1.5 \times 10^{-3}$ m are larger by about 84% and 90%, respectively, than those for particle diameter $d_p = 1 \times 10^{-3}$ m due to a reduction in the mass flow rate as the particle d_p diameter decreases (Figure 12). The magnitudes of u and v inside the bed at $y = 0.0015$ m for particle diameter $d_p = 1.5 \times 10^{-3}$ m are lower by about 90% and 90%, respectively, than those for particle diameter $d_p = 1 \times 10^{-3}$ m due to a reduction in the pressure as the particle diameter d_p increases. These results are shown Figures 9b and 10b.

To examine the flow fields at shorter times from the initiation, when the flow field has still not approached steady state, the same computations were made for $t = 1$ s. The results are qualitatively similar and were excluded for brevity but can be found in ref 21. The behavior is as expected, with the boundary layer thickening with time and the v velocity in the bed gradually dropping.

6.3. Heat- and Mass-Transfer Results in the Silica Gel. *6.3.1. Adsorption Process.* Parts a—d of Figure 11 show the time dependence at $x = 0.11$ m ($0.2L$ from the leading edge of the bed) of the desiccant surface water concentration, the surface temperature, and the overall averages of the water content and adsorption rate as computed by both models 1 and 2 (desiccant packed bed of spherical particles) with different particles and permeabilities. Having examined it under the same initial and boundary conditions, we found that the particle size in model 2

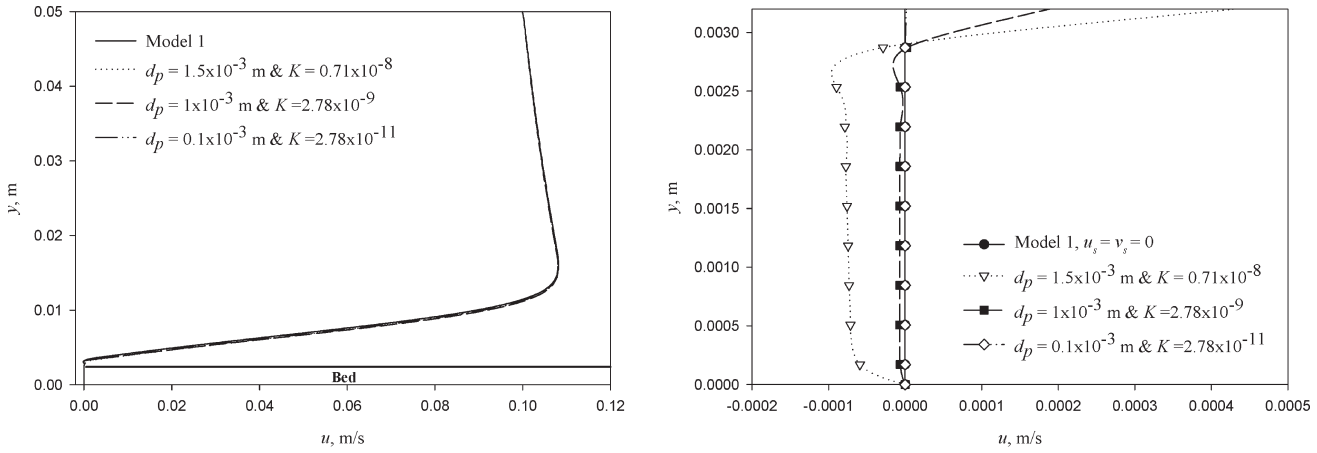

a. Over the bed **b.** Within the bed

Figure 9. u velocity profiles over and within the silica gel bed for model 2 as a function of y for different d_p (the model 1 results are overlapped by the $d_p = 0.1 \times 10^{-3}$ m curve). $u_\infty = 0.1$ m/s, $Re_L = 333$, $T_\infty = 30$ °C, $C_\infty = 0.0276$ kg/kg, $C_b = 0.003\,775$ kg/kg, $W_0 = 0.08$ kg/kg, $b = 0.00321$ m, $L = 0.05$ m, $h = 0.05$ m, $t = 60$ s, and $x = 0.125$ m.

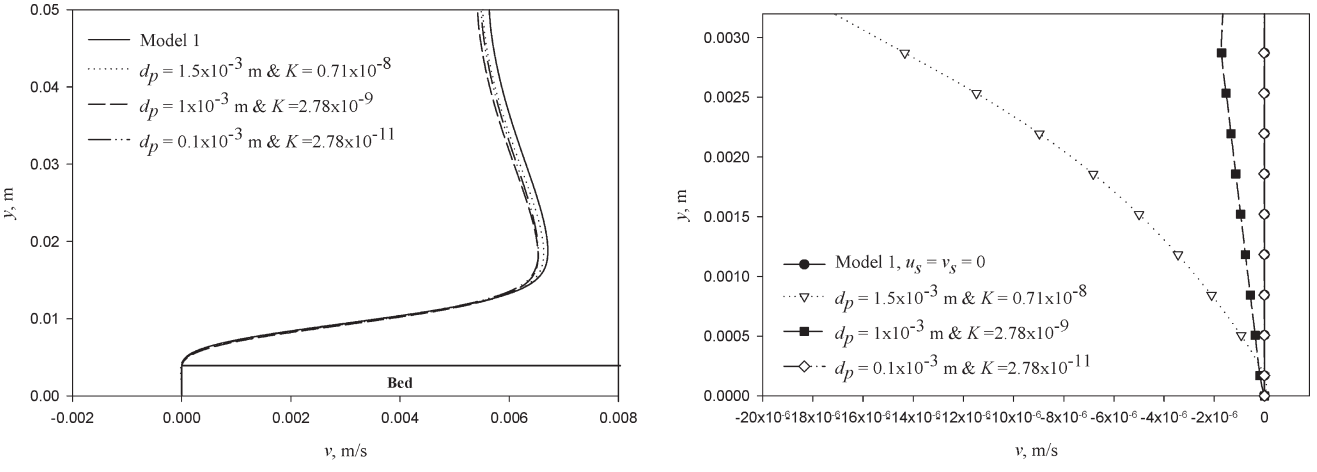

a. Over the bed **b.** Within bed

Figure 10. v velocity profiles over and within the silica gel bed for model 2, as a function of y for different d_p (the model 1 results are overlapped by the $d_p = 0.1 \times 10^{-3}$ m curve). $u_\infty = 0.1$ m/s, $Re_L = 333$, $T_\infty = 30$ °C, $C_\infty = 0.0276$ kg/kg, $C_b = 0.003\,775$ kg/kg, $W_0 = 0.08$ kg/kg, $b = 0.00321$ m, $L = 0.05$ m, $h = 0.05$ m, $t = 60$ s, and $x = 0.125$ m.

dx.doi.org/10.1021/ie102086s |*Ind. Eng. Chem. Res.* 2011, 50, 8859–8880

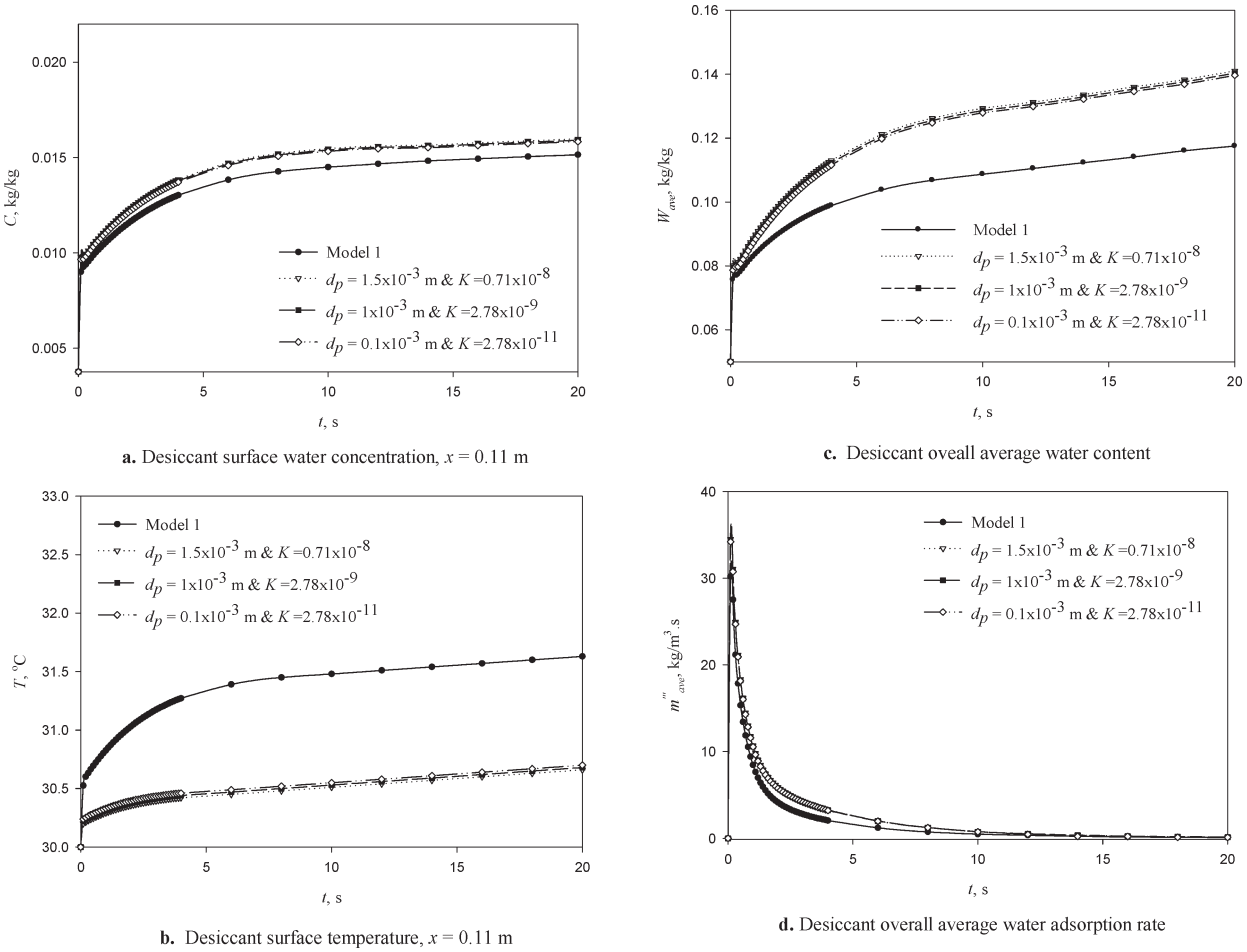

Figure 11. Dehumidification process of the time dependence of (a) the surface ($y = b$) concentration and the (b) surface temperature, (c) average water content, and (d) average water adsorption rate for models 1 and 2 with different particle diameters and permeabilities. $u_\infty = 0.1$ m/s, $Re_L = 333$, $T_\infty = 30$ °C, $C_\infty = 0.0276$ kg/kg, $C_b = 0.003\,775$ kg/kg, $W_0 = 0.05$ kg/kg, $L = 0.05$ m, $h = 0.05$ m, $b = 0.00321$ m, and $\sigma = 0.5$.

needs to be about 1×10^{-15} m to achieve approximately the same surface temperature, surface water concentration, water content, and water adsorption rate as attained by using model 1. The magnitudes of the surface water concentration and the averages of the water content and adsorption rate at 10 s that model 2 predicts with $d_p = 0.1 \times 10^{-3}$ m particles are about 5.2%, 15%, and 36%, respectively, larger than those computed by model 1 because of the increase in the mass flow rate that model 2 predicts (Figure 13). The magnitude of the surface temperature at 10 s computed by model 2 with $d_p = 0.1 \times 10^{-3}$ m is 0.95 °C lower than that computed by model 1 because of the presence of flow transport in the bed by convection for model 2. In model 2, the magnitudes of the averages of the water content and adsorption rate at 10 s increase by 1.1% and 1%, respectively, as d_p changes from 0.1×10^{-3} to 1.5×10^{-3} m, also because of the increase in the mass flow rate at the bed surface (Figure 13).

Silica gel reaches saturation when the water content is 38% at 100% ϕ (relative humidity), which is obtained at $T = 65.7$ °C and according to the silica gel isotherm (eq 19). The average maximal water content in this study is reached at $t = 20$ s, $b = 3.21$ mm, and $d_p = 1.5 \times 10^{-3}$ m and amounts to about 14%, as shown in Figure 11c, which indicates that the silica gel did not reach the saturation state and water condensation effects do not need to be considered in the model.

The results in Figure 11 are presented at $x = 0.11$ m ($0.2L$ from the leading edge of the bed), which is within the vicinity of the beginning of the bed, where most of the adsorption process occurs. Parts a−d of Figure 12 show the surface water concentration, temperature, water content, and water adsorption rate at $t = 4$ s for models 1 and 2 with different particles and permeabilities as a function of x. The water concentration and content decrease by about 49% and 60%, respectively, as x changes from 0.1 to 0.15 m because the adsorption rate increases rapidly by about 49% at the beginning of the bed from $x = 0.1$ m up to 0.106 m and then decays along the bed. The temperature increases 0.87 °C as x changes from 0.1 to 0.15 m because of the drop in the concentration and water content. It is noteworthy here that the concentration, water content, and adsorption rate increase and the temperature decreases slightly toward the end of x, in the vicinity of the trailing edge due to an increase in the u velocity gradient in the y direction, which causes an increase in the transport coefficient.

Parts a and b of Figure 13 depict the surface water mass flow rate along the bed as computed by models 1 and 2 with similar particle diameters and permeabilities but different times. At $x = 0.11$ m and $t = 20$ s, the magnitude of the mass flow rate for model 2, with $d_p = 0.1 \times 10^{-3}$ m, is about 58% larger than the magnitude predicted by model 1, which is due to an increase in the concentration gradient in the y direction. It also includes

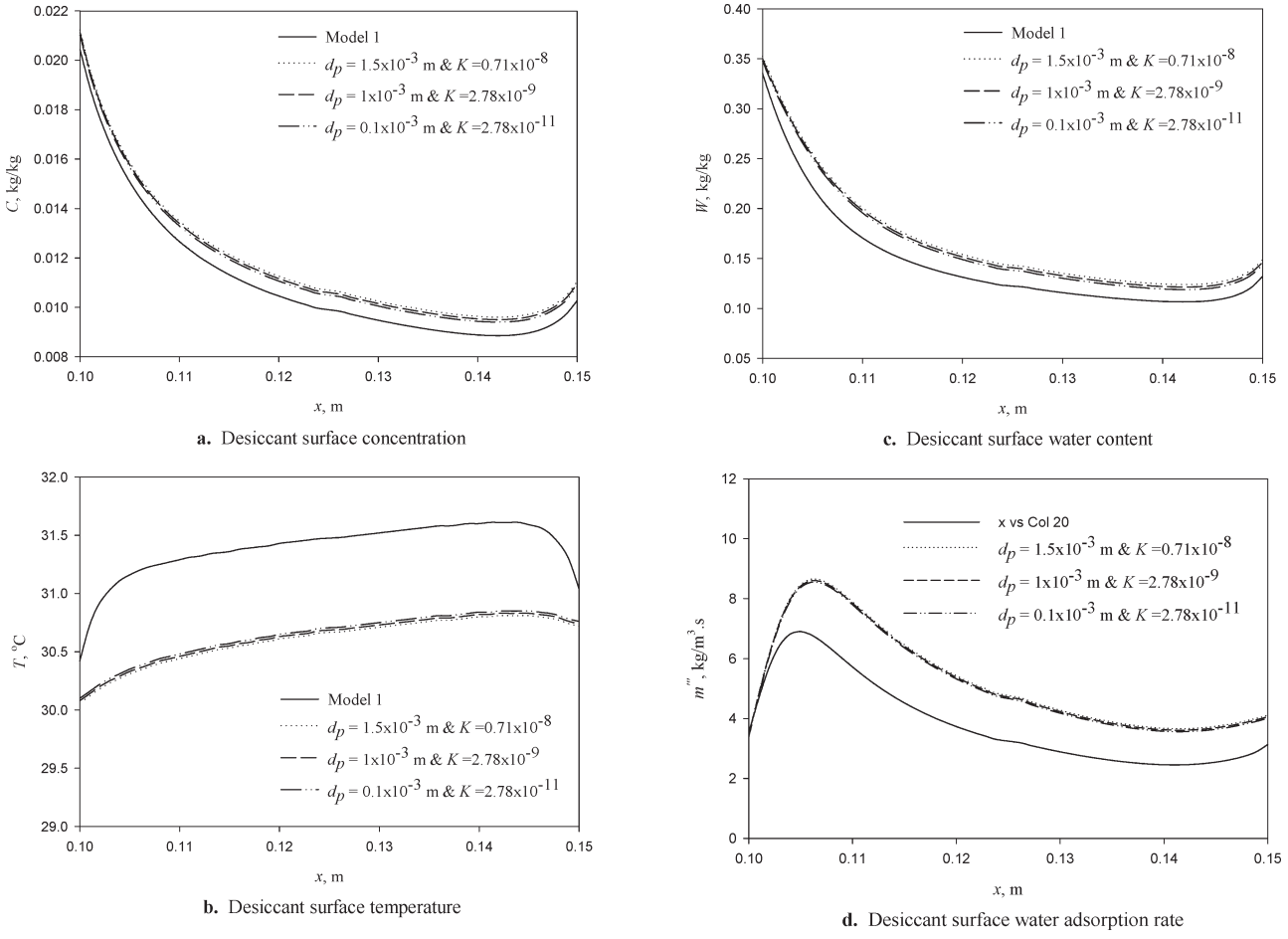

Figure 12. Dehumidification process of the surface ($y = b$) of (a) concentration, (b) temperature, (c) water content, and (d) water adsorption rate for models 1 and 2 with different particle diameters and permeabilities as a function of x. u_∞ = 0.1 m/s, Re_L = 333, T_∞ = 30 °C, C_∞ = 0.0276 kg/kg, C_b = 0.003775 kg/kg, W_0 = 0.05 kg/kg, L = 0.05 m, h = 0.05 m, b = 0.00321 m, t = 5 s, and σ = 0.5.

model 2's mass transport by convection, as shown in Figure 13a. In model 2, the magnitude of the mass flow rate at x = 0.11 m and t = 20 s increases by 2.7% as d_p increases from 0.1×10^{-3} to 1.5×10^{-3} m because of an increase in both the concentration gradient in the y direction and the water adsorption rate, as shown in Figure 13a. As the time changes from 1 to 20 s, the magnitude of the mass flow rate at x = 0.11 m for model 2 with $d_p = 1.5 \times 10^{-3}$ m decreases by about 21.3% because of the drop in the concentration gradient in the y direction at the desiccant bed surface with a time increase, as shown in Figure 13a,b. As seen in Figure 13, the water mass flow rate raises with x rapidly in the vicinity of the leading edge because the u velocity gradient in the y direction near the air—desiccant interface is large. Then, the water mass flow rate decays with x because of the corresponding reduction in the u velocity gradient in the y direction, which causes a reduction in the mass-transport coefficient.

6.3.1.1. Effective Diffusion Coefficient for the Adsorption Process. It is useful for practical desiccant design and use purposes to condense the detailed spatial and temporal numerical simulation into some simple average coefficients that can be used to easily predict dehumidification and regeneration rates. Model 2 allows the development and computation of an "effective diffusion coefficient" concept, here called $\overline{D}_{eff}$, from a basic composition of the desiccant, by equating the integral of the surface mass flow rate along the bed length as computed by model 2 to the integral of the mass flow rate as computed by model 1 through Fick's law

$$\int_x m_2'' \, dx = \rho_f \overline{D}_{eff} \int_x \left(\frac{\partial C}{\partial y}\right)_1 dx \tag{42}$$

so

$$\overline{D}_{eff} = \frac{\int_x m_2'' \, dx}{\rho_f \int_x \left(\frac{\partial C}{\partial y}\right)_1 dx} \tag{43}$$

The practical advantage of this approach is that the surface gradient $(\partial C/\partial y)_1$ can be calculated by using the much simpler model 1 and then combined with $\overline{D}_{eff}$, as shown by eq 42, to find the mass flux into or out of the desiccant. We then use the model 2 numerical results to derive a correlation of $\overline{D}_{eff}$ as a function of the flow Reynolds number and the desiccant particle diameter, which makes it easy to estimate the transport flux. Moreover, its determination allows easy evaluation of the effects of the convection inside the bed by a comparison with the ordinary diffusion coefficient, D_f, defining the ratio

$$\overline{\lambda} = \frac{\overline{D}_{eff}}{D_f} \tag{44}$$

dx.doi.org/10.1021/ie102086s |*Ind. Eng. Chem. Res.* 2011, 50, 8859–8880

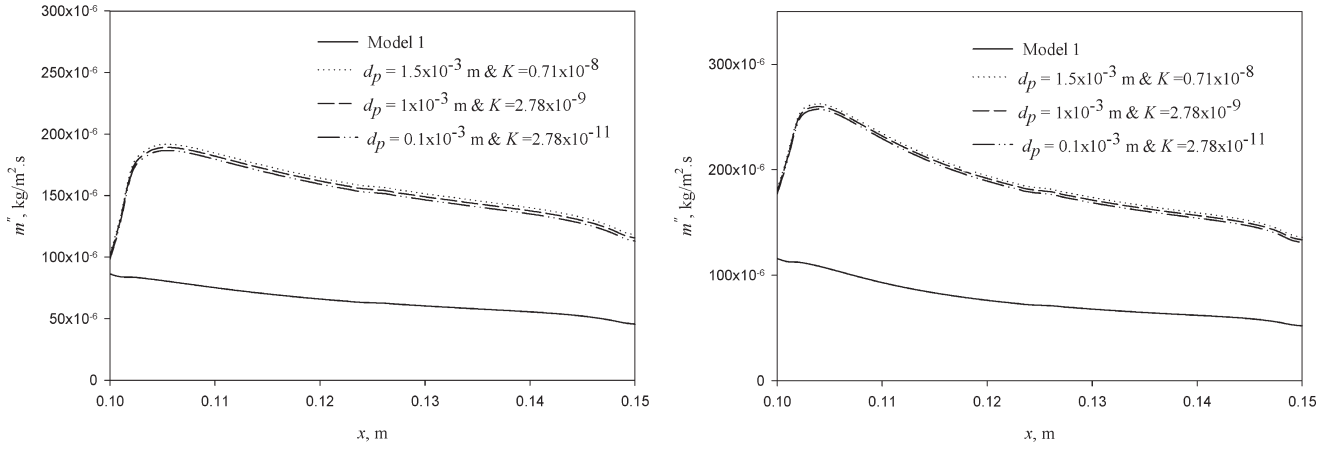

Figure 13. Dehumidification process of the surface water mass flow rate for models 1 and 2 with different particle diameters as a function of x and for two different times t = (a) 60 s and (b) 1 s. u_∞ = 0.1 m/s, Re_L = 333, T_∞ = 30 °C, C_∞ = 0.0276 kg/kg, C_b = 0.003 775 kg/kg, W_o = 0.05 kg/kg, L = 0.05 m, h = 0.05 m, b = 0.00321 m, and σ = 0.5.

Table 4. Dehumidification of the Integrated Effective Diffusion Coefficient $\overline{D}_{eff}$ and $\bar{\lambda}$ versus Particle Diameter d_p at t = 0.5 s (u_∞ = 0.1 m/s, Re_L = 333, T_∞ = 30 °C, C_∞ = 0.0276 kg/kg, C_b = 0.003 775 kg/kg, W_0 = 0.05 kg/kg, b = 0.00321 m, t = 20 s, and σ = 0.5)

particle diameter d_p, m	$\overline{D}_{eff}$, m^2/s	$\bar{\lambda}$
1.5×10^{-3}	1.154×10^{-4}	4.15
1×10^{-3}	1.13×10^{-4}	4.05
0.1×10^{-3}	1.087×10^{-4}	3.89

Table 5. Dehumidification of the Integrated Effective Diffusion Coefficient $\overline{D}_{eff}$ and $\bar{\lambda}$ versus Particle Diameter d_p at t = 10 s (u_∞ = 0.1 m/s, Re_L = 333, T_∞ = 30 °C, C_∞ = 0.0276 kg/kg, C_b = 0.003 775 kg/kg, W_0 = 0.05 kg/kg, b = 0.00321 m, t = 20 s, and σ = 0.5)

particle diameter d_p, m	$\overline{D}_{eff}$, m^2/s	$\bar{\lambda}$
1.5×10^{-3}	1.097×10^{-4}	3.93
1×10^{-3}	1.08×10^{-4}	3.87
0.1×10^{-3}	1.066×10^{-4}	3.82

where $\bar{\lambda}$ is the ratio between this integrated effective diffusion coefficient $\overline{D}_{eff}$ and the binary diffusion coefficient D_f for an air−water vapor mixture (here $D_f = 2.79 \times 10^{-5}$ m^2/s). Using eqs 43 and 44, with $(\partial C/\partial y)_1$ computed for the same conditions (u_∞ = 0.1 m/s, Re_L = 333, T_∞ = 30 °C, C_∞ = 0.0276 kg/kg, C_b = 0.003775 kg/kg, W_0 = 0.05 kg/kg, b = 0.00321 m, t = 20 s, and σ = 0.5) by model 1, we compute $\overline{D}_{eff}$ and $\bar{\lambda}$ for different d_p, at t = 0.5, 10, and 20 s, as shown in Tables 4−6.

We computed the magnitude of D_f along the bed surface as a function of x and the time, reflecting its change with temperature (eq 2.12 in ref 20) and found that it varied in the examined range of conditions by only about 4.66%, concluding that D_f can be considered a constant, about 26.6×10^{-6} m^2/s.

In addition to the surface-average value, it is also of important practical interest to examine the value and behavior of the *local* effective diffusion coefficient $D_{eff}(x,t)$, which is computed by the

Table 6. Dehumidification Integrated Effective Diffusion Coefficient $\overline{D}_{eff}$ and $\bar{\lambda}$ versus Particle Diameter d_p at t = 20 s (u_∞ = 0.1 m/s, Re_L = 333, T_∞ = 30 °C, C_∞ = 0.0276 kg/kg, C_b = 0.003 775 kg/kg, W_0 = 0.05 kg/kg, b = 0.00321 m, t = 20 s, and σ = 0.5)

particle diameter d_p, m	$\overline{D}_{eff}$, m^2/s	$\bar{\lambda}$
1.5×10^{-3}	1.07×10^{-4}	3.83
1×10^{-3}	1.052×10^{-4}	3.77
0.1×10^{-3}	1.01×10^{-4}	3.62

same principle,

$$D_{eff}(x,t) = \frac{m''_2(x,t)}{\rho_f \left(\dfrac{\partial C(x,t)}{\partial y}\right)_1} \tag{45}$$

and the local ratio $\lambda(x,t)$ between this local effective diffusion coefficient $D_{eff}(x,t)$ and the binary diffusion coefficient D_f is

$$\lambda(x,t) = \frac{D_{eff}(x,t)}{D_f} \tag{46}$$

Figure 14 shows the magnitude of $D_{eff}(x,t)$ along the bed surface as a function of x and the time for $d_p = 1.5 \times 10^{-3}$ and 1×10^{-3} m with Re = 333. They show that, as the time increases from 1 to 20 s, the magnitude of $D_{eff}(x,t)$ decreases along x because the concentration gradient in the y direction drops with time. A comparison of these results is presented in Table 7. The negative signs shown in Table 7 indicate a decrease in the percentage, whereas the positive signs imply an increase. It is also seen that the magnitude of $D_{eff}(x,t)$ rises along the bed across the time scale. It is seen to rise rapidly with x from the upstream edge at x = 0.1 m to x = 0.11 m because of the rapid rise in the mass flow rate into it in this region (Figure 13). The change in D_{eff} diminishes starting from x = 0.11 m up to x = 0.15 m because the mass flow rate decays slowly in this region (Figure 13). A comparative presentation of these results and those for the effects of time and flow Re are shown in Tables 7 and 8.

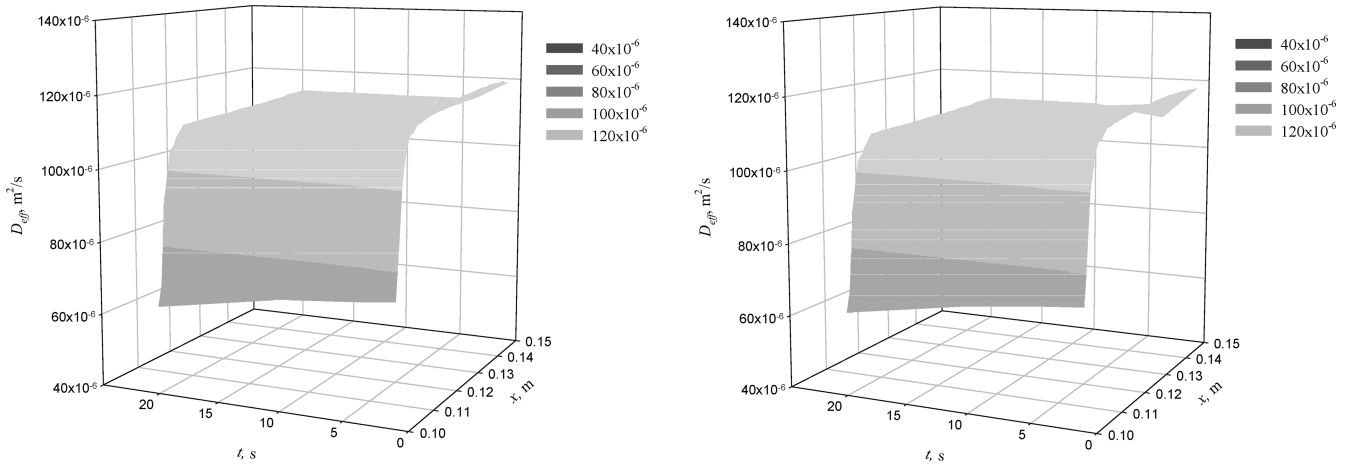

a. Particle diameter $d_p = 1.5 \times 10^{-3}$ m **b.** Particle diameter $d_p = 1 \times 10^{-3}$ m

Figure 14. Dehumidification process of the local effective diffusion coefficient D_{eff} as a function of x and t. u_∞ = 0.1 m/s, Re_L = 333, T_∞ = 30 °C, C_∞ = 0.0276 kg/kg, C_b = 0.003 775 kg/kg, W_0 = 0.08 kg/kg, L = 0.05 m, h = 0.05 m, b = 0.00321 m, and σ = 0.5.

Table 7. Change (%) in D_{eff} and λ for Different Time Ranges with Different x for the Adsorption Process in the Silica Gel Bed (u_∞ = 0.1 m/s, Re_L = 333, T_∞ = 30 °C, C_∞ = 0.0276 kg/kg, C_b = 0.003 775 kg/kg, W_0 = 0.05 kg/kg, L = 0.05 m, h = 0.05 m, b = 0.00321 m, and σ = 0.5)[a]

location	$\psi \times 100$, $d_p = 1.5 \times 10^{-3}$ m, Re = 333	$\zeta \times 100$, $d_p = 1.5 \times 10^{-3}$ m, Re = 333	$\psi \times 100$, $d_p = 1 \times 10^{-3}$ m, Re = 333	$\zeta \times 100$, $d_p = 1 \times 10^{-3}$ m, Re = 333	$\psi \times 100$, $d_p = 1.5 \times 10^{-3}$ m, Re = 1667	$\zeta \times 100$, $d_p = 1.5 \times 10^{-3}$ m, Re = 1667
t (1−20 s) at x = 0.1 m	−12	−12	−12.5	−12.5	−13	−13
t (1−20 s) at x = 0.11 m	−3.4	−3.4	−4.6	−4.6	−4	−4
t (1−20 s) at x = 0.15 m	−4.2	−4.2	−5.3	−5.3	−4.6	−4.6

[a] $\psi = [D_{eff}(x,t_L) - D_{eff}(x,t_s)]/D_{eff}(x,t_L)$ and $\zeta = [\lambda(x,t_L) - \lambda(x,t_s)]/\lambda(x,t_L)$, where t_L is the longer time and t_s is the shorter time.

Table 8. Change (%) in D_{eff} and λ for Different x with Different Time Ranges for the Adsorption Process in the Silica Gel Bed (u_∞ = 0.1 m/s, Re_L = 333, T_∞ = 30 °C, C_∞ = 0.0276 kg/kg, C_b = 0.003 775 kg/kg, W_0 = 0.05 kg/kg, L = 0.05 m, h = 0.05 m, b = 0.00321 m, and σ = 0.5)[a]

location	$\tau \times 100$, $d_p = 1.5 \times 10^{-3}$ m, Re = 333	$\omega \times 100$, $d_p = 1.5 \times 10^{-3}$ m, Re = 333	$\tau \times 100$, $d_p = 1 \times 10^{-3}$ m, Re = 333	$\omega \times 100$, $d_p = 1 \times 10^{-3}$ m, Re = 333	$\tau \times 100$, $d_p = 1.5 \times 10^{-3}$ m, Re = 1667	$\omega \times 100$, $d_p = 1.5 \times 10^{-3}$ m, Re = 1667
x (0.1−0.11 m) at t = 1 s	37	37	37.5	37.5	36	36
x (0.1−0.11 m) at t = 10	37.6	37.6	37.2	37.2	37	37
x (0.1−0.11 m) at t = 20 s	42.8	42.8	41	41	42	42
x (0.11−0.15 m) at t = 1 s	2.5	2.5	2	2	3	3
x (0.11−0.15 m) at t = 10 s	1.7	1.7	1.2	1.2	2	2
x (0.11−0.15 m) at t = 20 s	1.7	1.7	1	1	2	2

[a] $\tau = [D_{eff}(x_L,t) - D_{eff}(x_s,t)]/D_{eff}(x_L,t)$ and $\omega = [\lambda(x_L,t) - \lambda(x_s,t)]/\lambda(x_L,t)$, where x_L is the longer length and x_s is the shorter length.

Figure 15 shows the magnitude of $D_{eff}(x,t)$ along the bed surface as a function of x and time for $d_p = 1.5 \times 10^{-3}$ m and Re = 1667 in model 2. This figure shows that, as the time changes from 1 to 20 s, the magnitude of $D_{eff}(x,t)$ decreases along x because the concentration gradient in the y direction at the bed surface increases with the time increase, as shown in Figure 11a. A comparison of these results is presented in Table 7.

Figure 15 also indicates that the magnitude of $D_{eff}(x,t)$ rises as the bed length increases across the time scale. In other words, $D_{eff}(x,t)$ rises rapidly with x at the upstream edge, where x ranges from 0.1 to 0.11 m. This observation is due to the rapid rise in the mass flow rate into this region (Figure 13). The change in D_{eff} diminishes starting from x = 0.11 m up to x = 0.15 m because the mass flow rate decays slowly in this region (Figure 13). A comparison of these results is presented in Table 9.

In summary, D_{eff} rises rapidly with x at the upstream part of the bed, where the edge is at x = 0.1−0.11 m because of the rapid rise in the mass flow rate into it in this region (Figure 13). The change in

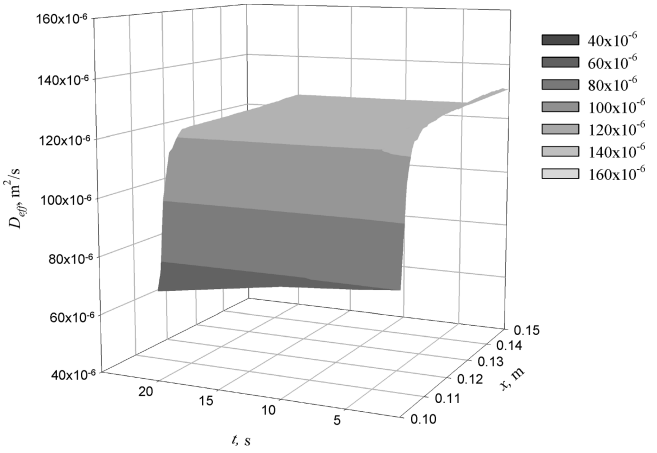

Figure 15. Dehumidification process of the local effective diffusion coefficient D_{eff} as a function of x and t. $u_\infty = 0.1$ m/s, $Re_L = 1667$, $T_\infty = 30$ °C, $C_\infty = 0.0276$ kg/kg, $C_b = 0.003\,775$ kg/kg, $W_0 = 0.05$ kg/kg, $L = 0.05$ m, $h = 0.05$ m, $b = 0.00321$ m, $\sigma = 0.5$, and $d_p = 1.5 \times 10^{-3}$ m.

D_{eff} diminishes starting from $x = 0.11$ m up to $x = 0.15$ m because the mass flow rate decays slowly in this region (Figure 13). Then, D_{eff} drops as the time changes from 1 to 20 s for the two particle diameters because of the drop in the concentration gradient at the bed surface with the time increases.

The results of the average ratio $\bar{\lambda}$ presented in Tables 4−6 and the local ratio $\lambda(x,t)$ at $x = 0.109$ m and $t = 1$ s (where the change in the ratio behavior is important) were correlated by us in the following equations as a function of the dimensionless particle diameter, D_p (d_p/b), in the range of 0.1×10^{-3} m $\le d_p \le 1.5 \times 10^{-3}$ m and Reynolds number, Re, in the range of $333 \le Re \le 1667$.

$$\bar{\lambda} = 2.66 {D_p}^{0.028} Re^{0.067} \quad (47)$$

$$\lambda(x,t) = 2.91 {D_p}^{0.0275} Re^{0.066} \quad (48)$$

6.3.2. Desorption Process. Water desorbs from a desiccant when it is heated, and we have analyzed this process by typically assuming that the drying air stream approached the desiccant bed at a temperature of 80 °C and a humidity concentration C = 0.015 (kg of water)/(kg of mixture) The desiccant was initially at $T = 80$ °C and $W = 0.135$ (kg of water)/kg of desiccant). Parts a−d of Figure 16 show the time dependence at $x = 0.11$ m ($0.2L$ from the leading edge of the bed) of the desiccant surface water concentration, surface temperature, and overall averages of the water content and desorption rate as computed by both models 1 and 2 with different particle diameters and permeabilities. The magnitudes of the surface water concentration and the averages of the water content and desorption rate at $t = 10$ s computed by model 2 with $d_p = 0.1 \times 10^{-3}$ m are about 10.3%, 8%, and 16.7%, respectively, smaller than those computed by model 1 because of the reduction in the mass flow rate that model 2 predicts. The magnitude of the surface temperature at $t = 10$ s computed by model 2 with $d_p = 0.1 \times 10^{-3}$ m is 0.95 °C larger than that computed by model 1 because of the presence of flow transport from the bed by convection for model 2. Also, the magnitudes of the surface water concentration and the averages of the water content and desorption rate at $t = 20$ s computed by model 2 with $d_p = 0.1 \times 10^{-3}$ m are about 20%, 13%, and 16.7%, respectively, smaller than those computed by model 1 because of the reduction in the mass flow rate that was obtained with model 2. The magnitude of the surface temperature at $t = 20$ s computed by model 2 with $d_p = 0.1 \times 10^{-3}$ m is 1 °C larger than that computed by model 1 because of the presence of flow transport from the bed by convection for model 2. In model 2, the magnitudes of the averages of the water content and desorption rate at $t = 10$ s decrease by 0.9% and 2%, respectively, as d_p increases from 0.1×10^{-3} to 1.5×10^{-3} m because of the decrease in the mass flow rate at the bed surface.

Table 9. Dehumidification of Integrated Effective Diffusion Coefficient $\bar{D}_{eff}$ and $\bar{\lambda}$ versus Particle Diameter d_p at Different Times in the Silica Gel Bed ($u_\infty = 0.1$ m/s, $Re_L = 1667$, $T_\infty = 30$ °C, $C_\infty = 0.0276$ kg/kg, $C_b = 0.003\,775$ kg/kg, $W_0 = 0.05$ kg/kg, $L = 0.05$ m, $h = 0.05$ m, $b = 0.00321$ m, $\sigma = 0.5$, and $d_p = 1.5 \times 10^{-3}$ m)

	$t = 0.5$ s		$t = 10$ s		$t = 20$ s	
particle diameter d_p, m	$\bar{D}_{eff}$, m^2/s	$\bar{\lambda}$	$\bar{D}_{eff}$ m^2/s	$\bar{\lambda}$	$\bar{D}_{eff}$, m^2/s	$\bar{\lambda}$
1.5×10^{-3}	8.23×10^{-5}	2.95	9.58×10^{-5}	3.43	1.05×10^{-4}	3.77
1×10^{-3}	7.95×10^{-5}	2.83	9.19×10^{-5}	3.3	1.01×10^{-4}	3.62
0.1×10^{-3}	7.72×10^{-5}	2.77	8.88×10^{-5}	3.18	9.58×10^{-5}	3.43

Parts a−d of Figure 17 show the surface water concentration, temperature, water content, and water desorption rate at $t = 5$ s for models 1 and 2 with different particles and permeabilities as a function of x. In model 2, the water concentration and water content increase by about 16.5% and 68%, respectively, as x changes from 0.1 to 0.15 m because the desorption rate decreases rapidly by about 57% at the beginning of the bed from $x = 0.1$ m up to 0.105 m and then increases along the bed. These increases in the water concentration and water content are due to an increase in the mass-transport coefficient along the bed, which is caused by an increase in the u velocity gradient in the y direction. The temperature decreases 0.54 °C as x changes from 0.1 to 0.15 m because of an increase in the concentration and water content. It is noteworthy here that the water concentration, water content, and desorption rate decrease and the temperature increases slightly toward the end of x, in the vicinity of the trailing edge, because of the reduction in the u velocity gradient in the y direction, which causes a decrease in the transport coefficient.

6.3.2.1. Effective Diffusion Coefficient for the Desorption Process. As we did for dehumidification, the integrated effective diffusion coefficient for the desorption process is computed using eqs 43 and 44, with $(\partial C/\partial y)_1$ computed for the same conditions ($u_\infty = 0.1$ m/s, $Re_L = 333$, $T_\infty = 80$ °C, $C_\infty = 0.015$ kg/kg, $C_b = 0.2$ kg/kg, $W_0 = 0.35$ kg/kg, $b = 3$ mm, $t = 60$ s, and $\sigma = 0.5$) by model 1. The results for $\bar{D}_{eff}$ and $\bar{\lambda}$ for different d_p at $t = 0.5$, 10, and 20 s are shown in Tables 9−11.

The local effective diffusion coefficient $D_{eff}(x,t)$ and the local $\lambda(x,t)$ are computed using eqs 45 and 46.

Figure 18 shows the magnitude of $D_{eff}(x,t)$ along the bed surface as a function of x and the time for $d_p = 1.5 \times 10^{-3}$ and 1×10^{-3} m in model 2 with $Re = 333$. Figure 18 depicts that, as the time changes from 1 to 20 s, the magnitude of $D_{eff}(x,t)$ increases all along x because the concentration gradient in the y direction increases at the bed surface as the time increases. A comparison of these results is presented in Table 10.

Figure 18 also depicts that the magnitude of $D_{eff}(x,t)$ drops along the bed length and increases with time. $D_{eff}(x,t)$ drops rapidly with x at the upstream part of the bed, from the upstream

edge at $x = 0.1-0.11$ m because of the rapid drop in the mass flow rate into it in this region. The change in D_{eff} diminishes starting from $x = 0.11$ m up to $x = 0.15$ m because the mass flow rate rises slowly in this region. A comparison of these results is presented in Table 11. The negative signs shown in Table 11 refer to the decreased percent change of the magnitude.

6.3.3. Model 2 for Laminar Flow in the Channel. Further analysis was made to examine the effect of the flow geometry on dehumidification, by performing analysis on a channel composed of two parallel desiccant plates. Figure 19 compares dehumidification over a flat plate desiccant and in a desiccant channel using model 2 with particle diameter $d_p = 1.5 \times 10^{-3}$ m and permeability $K = 0.7 \times 10^{-8}$. The average water contents for flow in a wide channel ($h = 0.05$ m) and a narrow channel ($h = 0.01$ m) are just about 2% and 7.4% (at $t = 20$ s), respectively, higher than those over a flat bed because of an increase in the u velocity gradient in the y direction in the channel. The u velocity gradients in the y direction in a wide channel and in a narrow channel are 9% and 17%, respectively, higher than the one over a flat bed, which caused an increase in the mass-transport coefficients.

6.4. Performance of the PSSASS Polymer Desiccant and Its Comparison with That of Silica Gel. *6.4.1. Desiccant Thermodynamic Isotherm and Performance.* A primary thermodynamic characteristic of a desiccant and its dehumidification and desorption effectiveness is its isotherm, which describes the relationship between the water content in the desiccant and the water vapor concentration at the local equilibrium at a constant temperature. Without going into details here, studies by Collier et al.[28] identified the type 1M (type I medium), S-shaped isotherm to be the most effective. The isotherm shape of the silica gel is closer to linear than to the type 1M, so other desiccants that have an isotherm similar to 1M are sought. One that is better in that way,[11] is polystyrenesulfonic acid sodium salt (PSSASS). The water uptake in the PSSASS polymer is about 40% at 60% RH, compared to the water uptake for the silica gel, which is only 30% at 60% RH, Applicability of PSSASS may require further improvement and modification,[29] but we have chosen it as an appropriate better desiccant for analysis and for comparison to silica gel.

6.4.2. PSSASS and Silica Gel Adsorption and Desorption Process Comparison. In a way identical with that performed for silica gel and shown in section 6.4.1, a detailed analysis of the heat and mass transfer and performance was also performed for PSSASS, and it was found that the trends of the results are the same as those for silica gel, but their magnitudes for PSSASS are higher because of its higher ability to absorb and desorb. Here we just describe the behavior of the effective diffusion coefficients for PSSASS, and upon comparison of major characteristics between

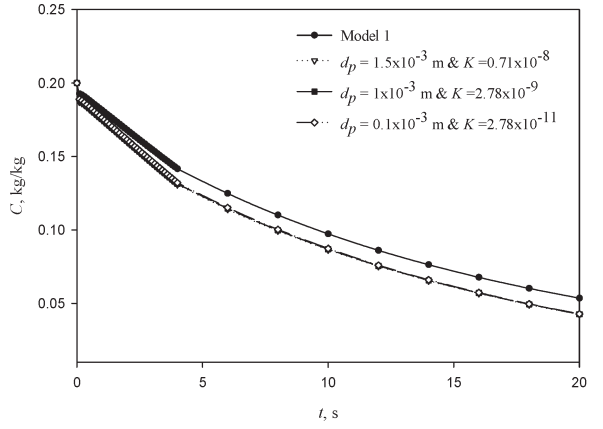

a. Desiccant surface water concentation, $x = 0.11$ m

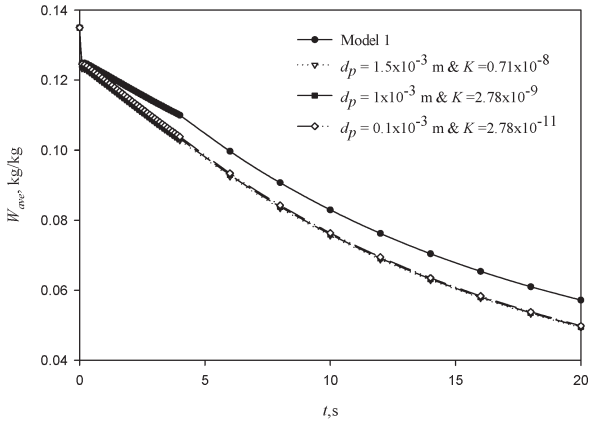

c. Desiccant overall average water content

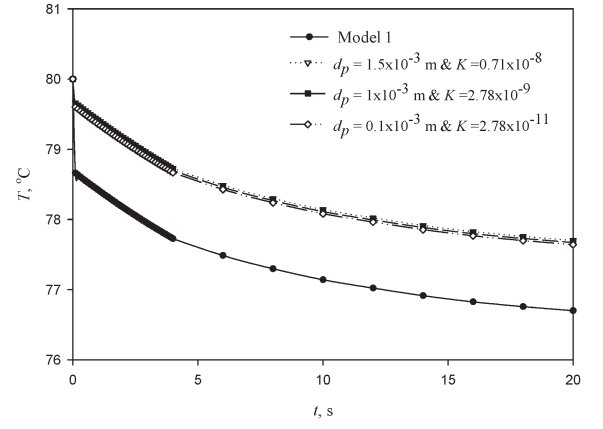

b. Desiccant surface temperature, $x = 0.11$ m

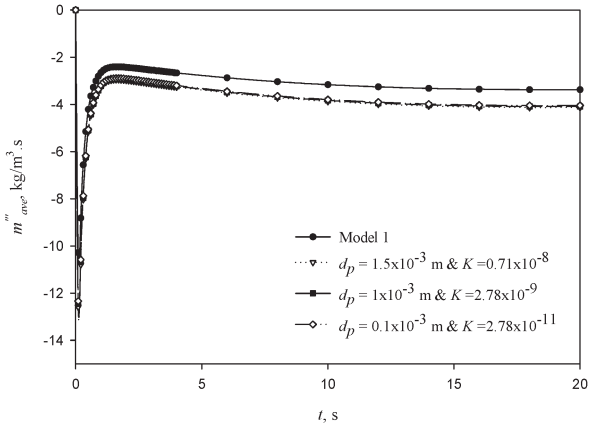

d. Desiccant overall average water desorption rate

Figure 16. Desorption process of the time dependence of the (a) surface ($y = b$) concentration, (b) surface temperature, (c) average water content, and (d) average desorption rate for models 1 and 2 with different particle diameters and permeabilities. $u_\infty = 0.1$ m/s, $Re_L = 333$, $T_\infty = 80$ °C, $C_\infty = 0.015$ kg/kg, $C_b = 0.2$ kg/kg, $W_0 = 0.135$ kg/kg, $L = 0.05$ m, $h = 0.05$ m, $b = 0.003\,21$ m, and $\sigma = 0.5$.

dx.doi.org/10.1021/ie102086s |*Ind. Eng. Chem. Res.* 2011, 50, 8859–8880

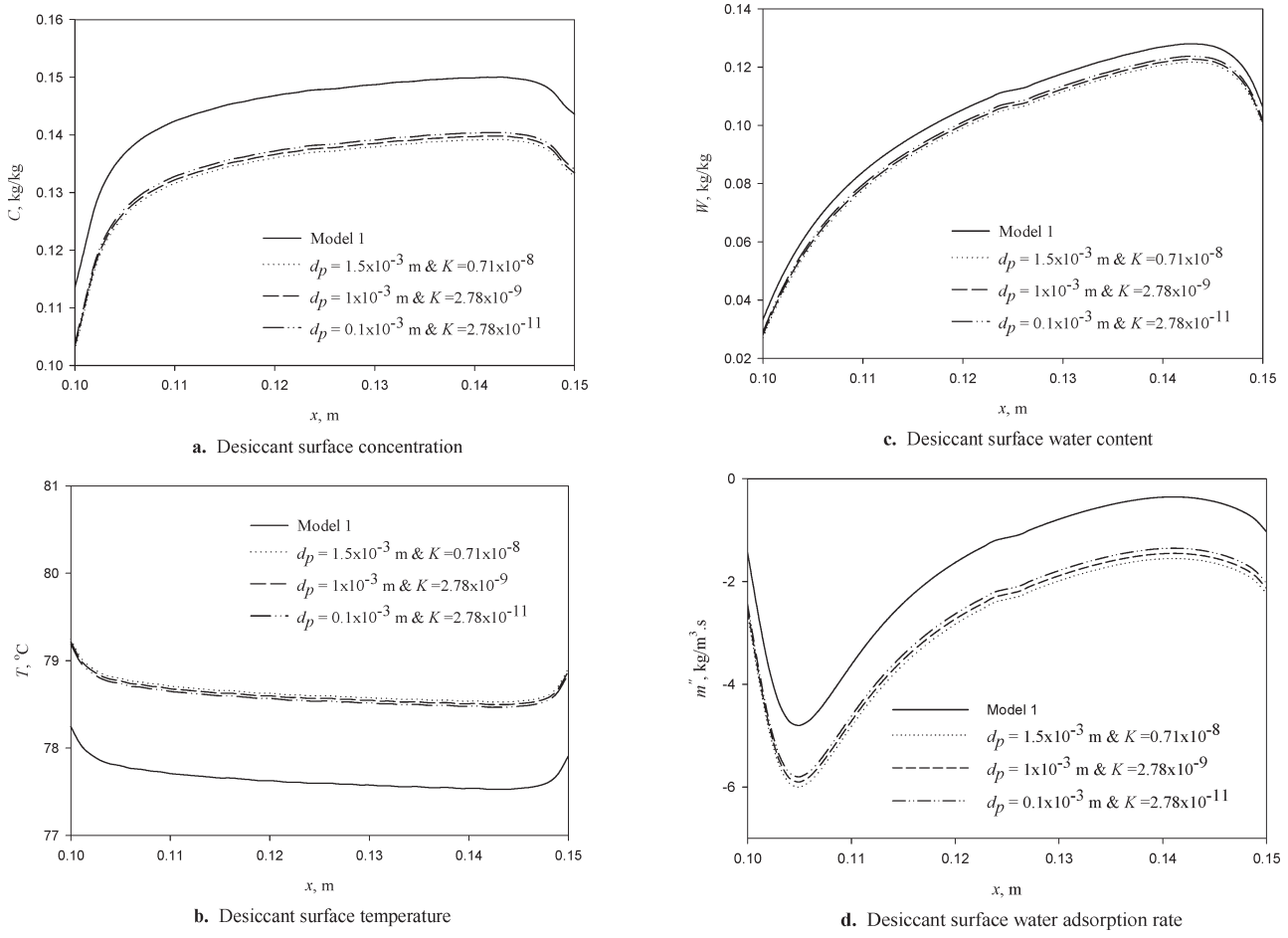

Figure 17. Desorption process of the surface ($y = b$) (a) concentration, (b) temperature, (c) water content, and (d) water desorption rate for models 1 and 2 with different particle diameters and permeabilities as a function of x. $u_\infty = 0.1$ m/s, $Re_L = 333$, $T_\infty = 80$ °C, $C_\infty = 0.015$ kg/kg, $C_b = 0.2$ kg/kg, $W_0 = 0.135$ kg/kg, $L = 0.05$ m, $h = 0.05$ m, $b = 0.00321$ m, $t = 5$ s, and $\sigma = 0.5$.

Table 10. Change (%) in the D_{eff} and λ for Different Time Ranges with Different x for the Adsorption Process in the Silica Gel Bed ($u_\infty = 0.1$ m/s, $Re_L = 333$, $T_\infty = 30$ °C, $C_\infty = 0.0276$ kg/kg, $C_b = 0.003\,775$ kg/kg, $W_0 = 0.05$ kg/kg, $L = 0.05$ m, $h = 0.05$ m, $b = 0.00321$ m, and $\sigma = 0.5$)[a]

location	$\psi \times 100$, $d_p = 1.5 \times 10^{-3}$ m	$\zeta \times 100$, $d_p = 1.5 \times 10^{-3}$ m	$\psi \times 100$, $d_p = 1 \times 10^{-3}$ m	$\zeta \times 100$, $d_p = 1 \times 10^{-3}$ m
t (1−20 s) at $x = 0.1$ m	1.8	1.8	1.3	1.3
t (1−20 s) at $x = 0.11$ m	31	31	29	29
t (1−20 s) at $x = 0.15$ m	12	12	11	11

[a] $\psi = [D_{eff}(x,t_L) - D_{eff}(x,t_s)]/D_{eff}(x,t_L)$ and $\zeta = [\lambda(x,t_L) - \lambda(x,t_s)]/\lambda(x,t_L)$, where t_L is the longer time and t_s is the shorter time.

Table 11. Change (%) in D_{eff} and λ for Different x with Different Time Ranges for the Desorption Process in the Silica Gel Bed ($u_\infty = 0.1$ m/s, $Re_L = 333$, $T_\infty = 80$ °C, $C_\infty = 0.015$ kg/kg, $C_b = 0.2$ kg/kg, $W_0 = 0.135$ kg/kg, $L = 0.05$ m, $h = 0.05$ m, $b = 0.00321$ m, and $\sigma = 0.5$)[a]

location	$\tau \times 100$, $d_p = 1.5 \times 10^{-3}$ m	$\omega \times 100$, $d_p = 1.5 \times 10^{-3}$ m	$\tau \times 100$, $d_p = 1 \times 10^{-3}$ m	$\omega \times 100$, $d_p = 1 \times 10^{-3}$ m
x (0.1−0.11 m) at $t = 1$ s	−51	−51	−49	−49
x (0.1−0.11 m) at $t = 10$	−40	−40	−38	−38
x (0.1−0.11 m) at $t = 20$ s	−30	−30	−27	−27
x (0.11−0.15 m) at $t = 1$ s	−2.7	−2.7	−2.5	−2.5
x (0.11−0.15 m) at $t = 10$ s	−10	−10	−8	−8
x (0.11−0.15 m) at $t = 20$ s	−20	−20	−18	−18

[a] $\tau = [D_{eff}(x_L,t) - D_{eff}(x_s,t)]/D_{eff}(x_L,t)$ and $\omega = [\lambda(x_L,t) - \lambda(x_s,t)]/\lambda(x_L,t)$, where x_L is the longer length and x_s is the shorter length.

dx.doi.org/10.1021/ie102086s |Ind. Eng. Chem. Res. 2011, 50, 8859–8880

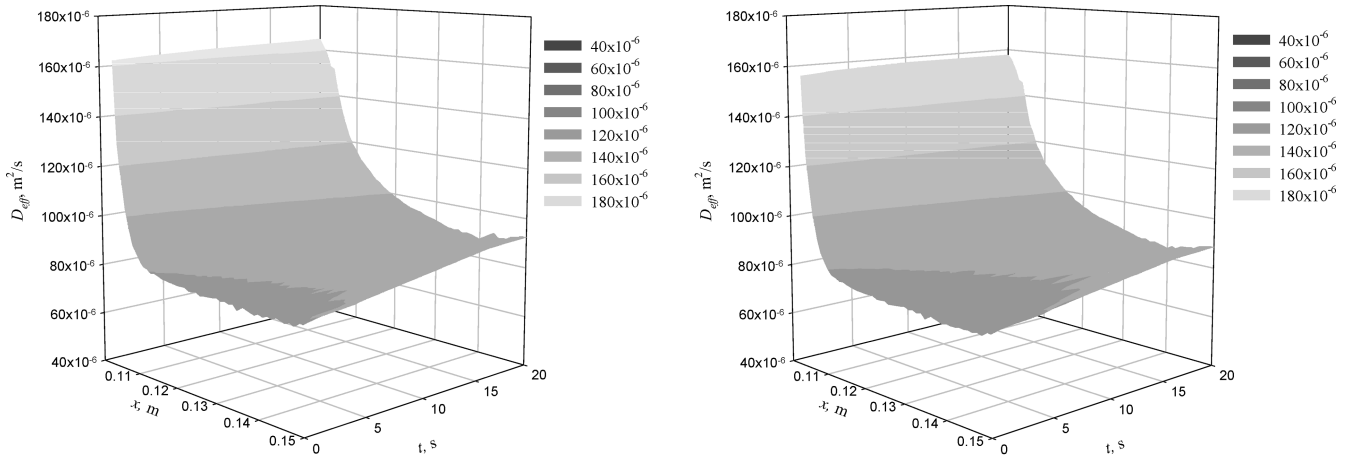

a. Particle diameter d_p = 1.5x10^{-3} m

b. Particle diameter d_p = 1x10^{-3} m

Figure 18. Desorption process of the local effective diffusion coefficient D_{eff} as a function of x and t. u_∞ = 0.1 m/s, Re_L = 333, T_∞ = 80 °C, C_∞ = 0.015 kg/kg, C_b = 0.2 kg/kg, W_0 = 0.135 kg/kg, L = 0.05 m, h = 0.05 m, b = 0.00321 m, and σ = 0.5.

the two desiccants, further detailed results for PSSASS can be found in ref 21.

In the dehumidification process, $\overline{D}_{eff}$ and $\bar{\lambda}$ for different d_p at t = 0.5, 10, and 20 s are shown in Table 12. Figure 20 shows the magnitude of $D_{eff}(x,t)$ along the bed surface as a function of x and the time for $d_p = 1.5 \times 10^{-3}$ and 1×10^{-3} m in model 2 with Re = 333. The observed trends are very similar to those of $D_{eff}(x,t)$ with silica gel. A comparison of these results is presented in Table 13. The negative signs in this table indicate a decrease in percentage, whereas the positive signs imply an increase.

Figure 21 shows the magnitude of $D_{eff}(x,t)$ and along the bed surface as a function of x and the time for $d_p = 1.5 \times 10^{-3}$ and 1×10^{-3} m in model 2 with Re = 333. The summary of the integrated effective diffusion coefficient $\overline{D}_{eff}$ computed for the silica gel and PSSASS polymer with different particle diameters at t = 20 s is presented in Table 14.

It is found that the magnitude of the effective diffusion coefficient in the adsorption/desorption processes for both silica gel and the PSSASS polymer with 0.1×10^{-3} m is larger by 73%/70% and 80%/72%, respectively, of the magnitude of the water vapor−air (binary) diffusion coefficient ($D_f = 2.79 \times 10^{-5}$ m/s). The results of the average ratio $\bar{\lambda}$ and the local ratio $\lambda(x,t)$ in the adsorption process are correlated as a function of the dimensionless particle diameter, D_p, and Reynolds number, Re, for silica gel (eqs 47 and 48).

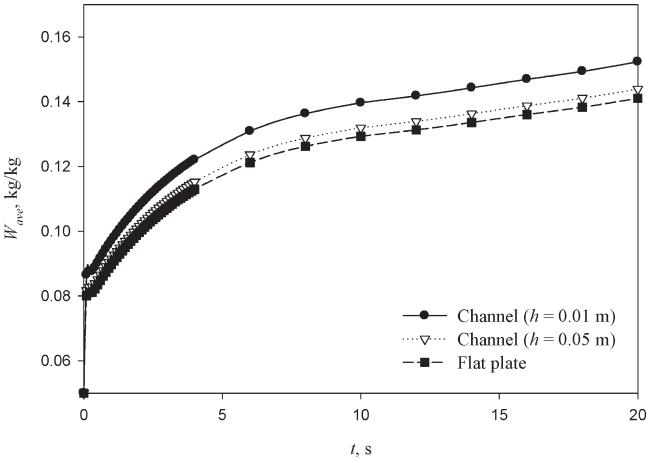

Figure 19. Time dependence of the average water content of model 2 for a plate desiccant and for two desiccant channel widths (h). u_∞ = 0.1 m/s, Re_L = 333, T_∞ = 30 °C, C_∞ = 0.0276 kg/kg, C_b = 0.003 775 kg/kg, W_0 = 0.05 kg/kg, b = 0.00321 m, σ = 0.5, $d_p = 1.5 \times 10^{-3}$ m, and $K = 0.71 \times 10^{-8}$.

Parts a−d of Figure 22 show heat- and mass-transfer comparisons as a function of x and t between the two desiccants, and they are basically self-explanatory. For comparison, the initial water concentrations for the two beds must be different in order to make the initial water contents for both the silica gel and PSSASS beds the same, and they are computed using the local equilibrium relations (isotherm shape, eqs 19 and 20). The initial water content computation starts by inserting the initial concentration in eq 17 and solving for the relative humidity. Then, the relative humidity is substituted into the local equilibrium relation (isotherm shape, eqs 19 and 20), and the equations are solved for the water content. The initial concentration for silica gel is thus made 65.5% larger than PSSASS. The magnitude of the silica gel surface water concentration at t = 20 s is about 73.5% larger than that for PSSASS because the local equilibrium relations (isotherm shape) for the two desiccants are different and the initial water content needs to be the same in both beds.

All of the results show that PSSASS has higher adsorption and desorption rates than silica gel because of both the smaller thermal diffusivity of silica gel (the thermal diffusivity α is

Table 12. Dehumidification of Integrated Effective Diffusion Coefficient $\overline{D}_{eff}$ and $\bar{\lambda}$ versus Particle Diameter d_p at Different Times in the PSSASS Bed (u_∞ = 0.1 m/s, Re_L = 333, T_∞ = 30 °C, C_∞ = 0.0276 kg/kg, C_b = 0.0013 kg/kg, W_0 = 0.05 kg/kg, L = 0.05 m, h = 0.05 m, b = 0.00321 m, and σ = 0.5)

	t = 0.5 s		t = 10 s		t = 20 s	
particle diameter d_p, m	$\overline{D}_{eff}$, m^2/s	$\bar{\lambda}$	$\overline{D}_{eff}$, m^2/s	$\bar{\lambda}$	$\overline{D}_{eff}$, m^2/s	$\bar{\lambda}$
1.5×10^{-3}	1.7×10^{-4}	6.09	1.59×10^{-4}	5.7	1.575×10^{-4}	5.64
1×10^{-3}	1.6×10^{-4}	5.73	1.56×10^{-4}	5.6	1.55×10^{-4}	5.56
0.1×10^{-3}	1.52×10^{-4}	5.45	1.52×10^{-4}	5.48	1.48×10^{-4}	5.3

dx.doi.org/10.1021/ie102086s |Ind. Eng. Chem. Res. 2011, 50, 8859–8880

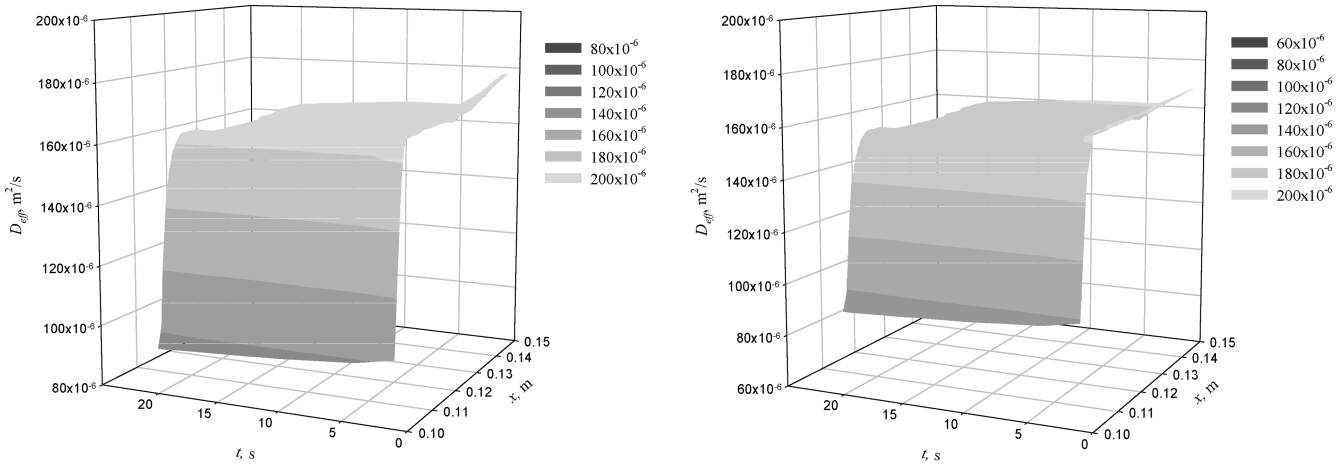

a. Particle diameter d_p = 1.5x10^{-3} m

b. Particle diameter d_p = 1x10^{-3} m

Figure 20. PSSASS dehumidification process of the local effective diffusion coefficient D_{eff} as a function of x and t. u_∞ = 0.1 m/s, Re_L = 333, T_∞ = 30 °C, C_∞ = 0.0276 kg/kg, C_b = 0.0013 kg/kg, W_0 = 0.05 kg/kg, L = 0.05 m, h = 0.05 m, b = 0.00321 m, and σ = 0.5.

Table 13. Change (%) in D_{eff} and λ for Different Time Ranges with Different x for the Adsorption Process in the PSSASS Bed (u_∞ = 0.1 m/s, Re_L = 333, T_∞ = 30 °C, C_∞ = 0.0276 kg/kg, C_b = 0.0013 kg/kg, W_0 = 0.05 kg/kg, L = 0.05 m, h = 0.05 m, b = 0.00321 m, and σ = 0.5)[a]

location	$\psi \times 100$, d_p= 1.5 × 10^{-3} m, Re = 333	$\zeta \times 100$, d_p= 1.5 × 10^{-3} m, Re = 333	$\psi \times 100$, d_p = 1 × 10^{-3} m, Re = 333	$\zeta \times 100$, d_p= 1 × 10^{-3} m, Re = 333	$\psi \times 100$, d_p= 1.5 × 10^{-3} m, Re = 1667	$\zeta \times 100$, d_p= 1.5 × 10^{-3} m, Re = 1667
t (1−20 s) at x = 0.1 m	−6.3	−6.3	−6	−6	−7	−7
t (1−20 s) at x = 0.11 m	−4.7	−4.7	−3.6	−3.6	−5	−5
t (1−20 s) at x = 0.15 m	−8.4	−8.4	−5.9	−5.9	−9	−9

[a] $\psi = [D_{eff}(x,t_L) - D_{eff}(x,t_s)]/D_{eff}(x,t_L)$ and $\zeta = [\lambda(x,t_L) - \lambda(x,t_s)]/\lambda(x,t_L)$, where t_L is the longer time and t_s is the shorter time.

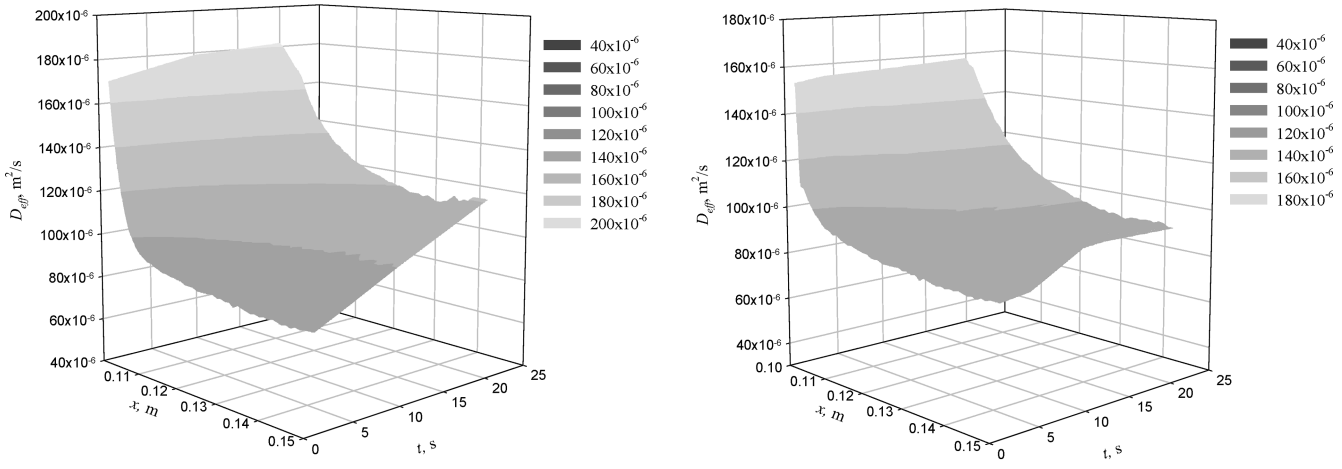

a. Particle diameter d_p = 1.5x10^{-3} m

b. Particle diameter d_p = 1x10^{-3} m

Figure 21. PSSASS desorption process of the local effective diffusion coefficient D_{eff} as a function of x and t. u_∞ = 0.1 m/s, Re_L = 333, T_∞ = 80 °C, C_∞ = 0.015 kg/kg, C_b = 0.055 kg/kg, W_0 = 0.135 kg/kg, L = 0.05 m, h = 0.05 m, b = 0.00321 m, and σ = 0.5.

1.38 × 10^{-7} m^2/s for silica gel and 8.6 × 10^{-6} m^2/s for PSSASS) and an increase in the water content of the PSSASS polymer according to the PSSASS local equilibrium relation (isotherm shape, eq 20; Table 15).

dx.doi.org/10.1021/ie102086s |Ind. Eng. Chem. Res. 2011, 50, 8859–8880

Parts a−d of Figure 23 show the time dependence at $x = 0.11$ m ($0.2L$ from the leading edge of the bed) of the desiccant surface water concentration, surface temperature, and overall averages of the water content and desorption rate of model 2 for silica gel with variable properties and PSSASS. The magnitudes of the silica gel surface water concentration at $t = 10$ and 20 s are about 73% and 73.8%, respectively, smaller than those for PSSASS because the local equilibrium relations for the two desiccants are different and the initial water content needs to be the same in both beds. The magnitudes of the surface temperature and the overall averages of the water content and desorption rate in the silica gel bed at $t = 10$ s are 1.06 °C, 7.4%, and 31%, respectively, larger than those in the PSSASS bed, whereas the magnitudes at $t = 20$ s are 1.1 °C, 11%, and 31%, respectively, larger than those in PSSASS because of both the decreased thermal diffusivity of silica gel and the variation between the silica gel and PSSASS equilibrium relations (isotherm shape).

Table 14. Integrated Effective Diffusion Coefficient $\overline{D}_{eff}$ for Silica Gel and PSSASS versus Particle Diameter d_p at $t = 20$ s

	$\overline{D}_{eff}$,[a] m^2/s	
particle diameter d_p, m	silica gel	PSSASS
1.5×10^{-3}	1.07×10^{-4} (A)	1.575×10^{-4} (A)
	1.05×10^{-4} (D)	1.33×10^{-4} (D)
1×10^{-3}	1.052×10^{-4} (A)	1.55×10^{-4} (A)
	1.01×10^{-4} (D)	1.11×10^{-4} (D)
0.1×10^{-3}	1.01×10^{-4} (A)	1.48×10^{-4} (A)
	9.56×10^{-5} (D)	9.85×10^{-5} (D)

[a] A is adsorption, and D is desorption.

Parts a−d of Figure 24 show the surface water concentration, temperature, water content, and water desorption rate of model 2 at $t = 4$ s for silica gel with variable properties and PSSASS as a function of x. The magnitudes of the silica gel surface water concentration at $x = 0.11$ m is about 73% smaller than that for PSSASS because the local equilibrium relations for the two desiccants are different and the initial water content needs to be the same in both beds. The magnitudes of the surface temperature and the overall averages of the water content and desorption rate in the silica gel bed at $x = 0.11$ m are 1.04 °C, 8%, and 19%, respectively, larger than those in the PSSASS bed because of both the decrease in the thermal diffusivity of silica gel and the variation between the silica gel and PSSASS equilibrium relations (isotherm shape).

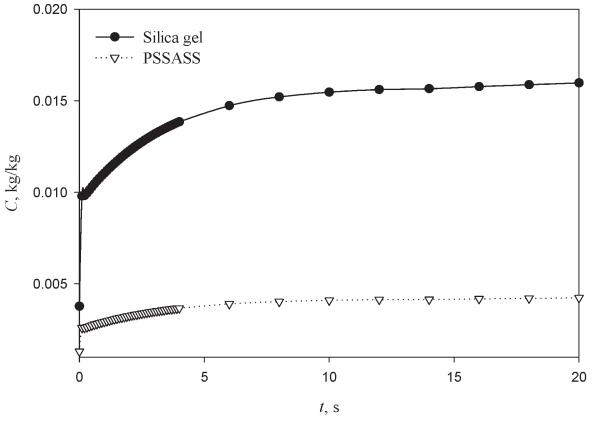

a. Desiccant surface water concentration, $x = 0.11$ m

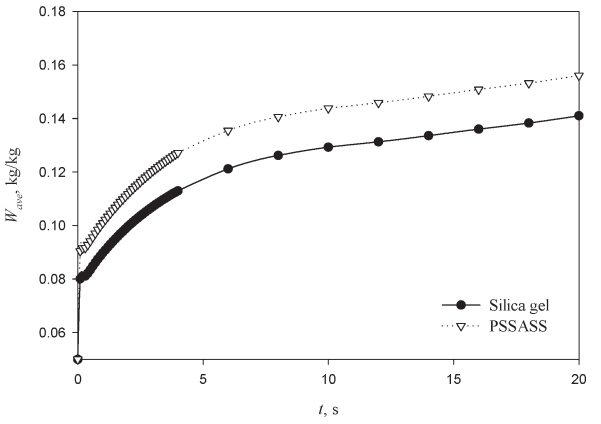

c. Desiccant overall average water content

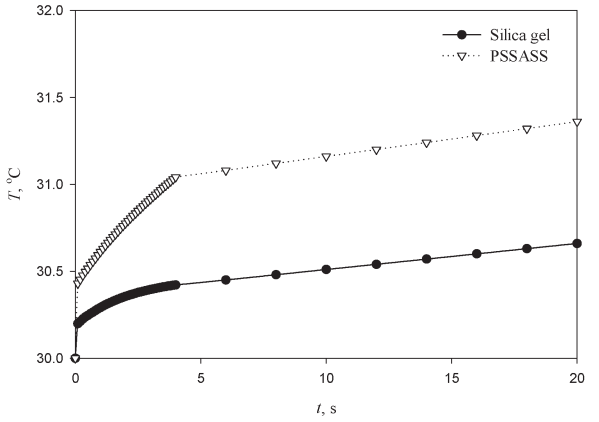

b. Desiccant surface temperature, $x = 0.11$ m

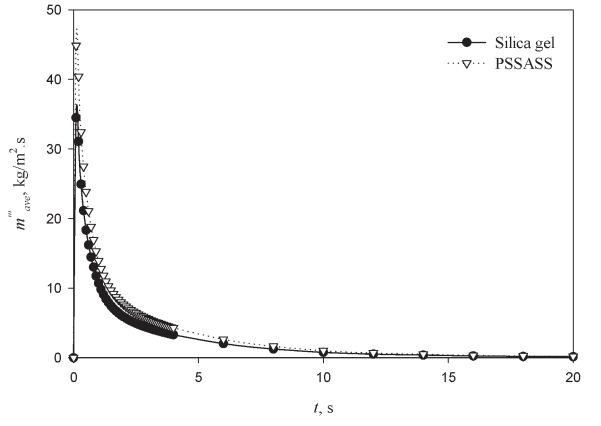

d. Desiccant overall average water adsorption rate

Figure 22. Time dependence of the desiccant (a) surface ($y = b$) water concentration, (b) surface temperature, (c) average water content, and (d) average water adsorption rate of model 2 for two different desiccants in the adsorption process. $u_\infty = 0.1$ m/s, $Re_L = 333$, $T_\infty = 30$ °C, $C_\infty = 0.0276$ kg/kg, $C_b = 0.0013$ (PSSASS) and 0.003775 (silica gel) kg/kg, $W_0 = 0.05$ kg/kg, $L = 0.05$ m, $h = 0.05$ m, $b = 0.00321$ m, $\sigma = 0.5$, $d_p = 1.5 \times 10^{-3}$ m, and $K = 0.71 \times 10^{-8}$.

dx.doi.org/10.1021/ie102086s |Ind. Eng. Chem. Res. 2011, 50, 8859–8880

7. CONCLUSIONS

A more rigorous conjugate-transient two-dimensional numerical model (model 2) of solid bed desiccant systems (plates and narrow channels) used for dehumidification of a gas laminarly flowing along the desiccant, which, importantly, includes associated transport through the desiccant body, was developed and validated. This improvement of the basic understanding of the process can be used for an easier determination of ways for improving the overall performance of such materials and systems. The solution provided a detailed exposition of the associated heat- and mass-transfer phenomena and of the desiccant performance, conducted here for both the absorption and desorption processes in a range of air-flow Reynolds numbers and desiccant bed particle sizes and for two types of desiccant materials, silica gel and PSSASS polymer. The results were also compared to those from the authors' simpler model (model 1) that was published earlier and that does not consider transport through the solid desiccant.

Model 2 was also employed to define and compute an "effective diffusion coefficient" from the basic composition of the desiccant, which is useful for characterizing desiccant properties and behavior in practical analysis. Besides the detailed behavior, some of the practical results are as follows: (i) the adsorption/desorption processes occur much faster at the flow entrance region; (ii) the mass-transport rates increase with the Reynolds number; (iii) within the studied range, manufacturing of the solid desiccant from larger particles raises its mass-transport rates; (iv) the water content and adsorption rate for PSSASS are larger than those of silica gel, thus making PSSASS a more effective desiccant than silica gel.

For the silica gel bed, in the adsorption process, the overall average water content computed by model 2 is larger by about 15%, and in desorption, it is smaller by 13%, than those predicted by Model 1, both because of an increase in the mass flow rate that model 2 predicts.

Table 15. Adsorption/Desorption Results in Silica Gel and the PSSASS Polymer Bed[a]

desiccant material	$\psi \times 100$	$\zeta \times 100$
model 2 (silica gel)	1.1% (A)	1% (A)
$d_p = (0.1-1.5) \times 10^{-3}$ m	−0.9% (D)	−2% (D)
model 2 (PSSASS)	1% (A)	0.95% (A)
$d_p = (0.1-1.5) \times 10^{-3}$ m	−1.98% (D)	−6.3% (D)

[a] A is adsorption, and D is desorption. $\psi = [W(d_p^L) - W(d_p^s)]/W(d_p^L)$ and $\zeta = [m'''(d_p^L) - m'''(d_p^s)]/m'''(d_p^L)$, where d_p^L is the large particle diameter and d_p^s is the small particle diameter.

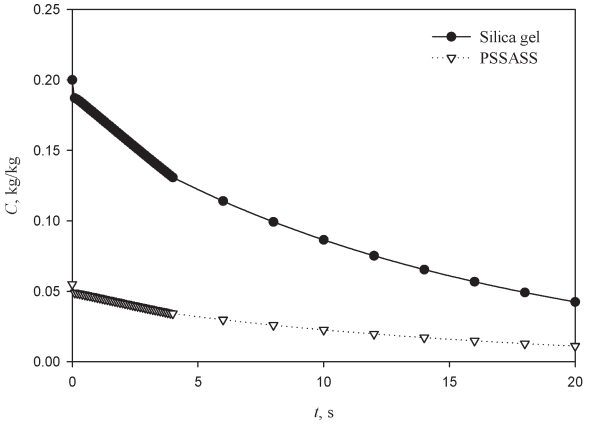

a. Desiccant surface water concentation, $x = 0.11$ m

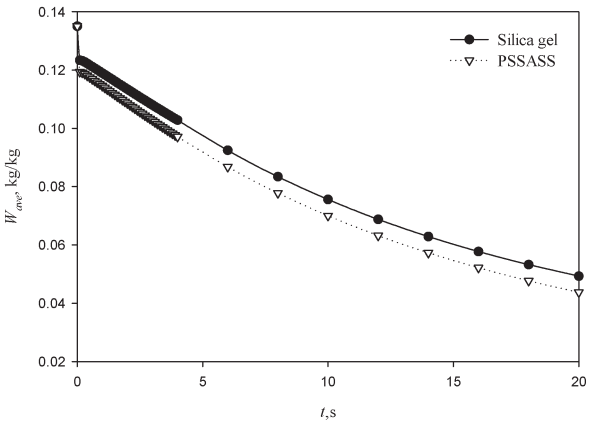

c. Desiccant overall average water content

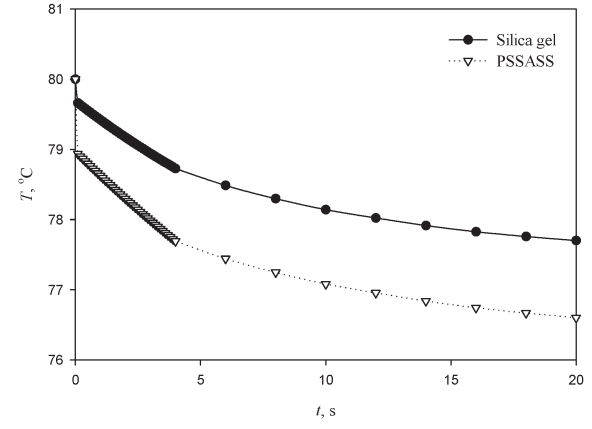

b. Desiccant surface temperature, $x = 0.11$ m

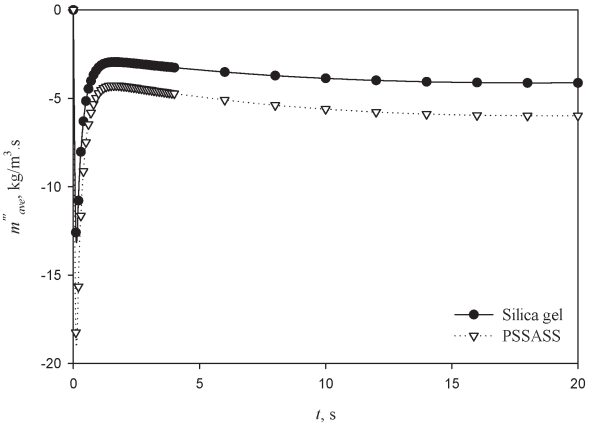

d. Desiccant overall average water desorption rate

Figure 23. Time dependence of the desiccant (a) surface ($y = b$) water concentration, (b) surface temperature, (c) average water content, and (d) average water desorption rate of model 2 for two different desiccants in the desorption process. $u_\infty = 0.1$ m/s, $Re_L = 333$, $T_\infty = 30$ °C, $C_\infty = 0.015$ kg/kg, $C_b = 0.055$ (PSSASS) and 0.2 (silica gel) kg/kg, $W_0 = 0.135$ kg/kg, $L = 0.05$ m, $h = 0.05$ m, $b = 0.003\,21$ m, $\sigma = 0.5$, $d_p = 1.5 \times 10^{-3}$ m, and $K = 0.71 \times 10^{-8}$.

dx.doi.org/10.1021/ie102086s |Ind. Eng. Chem. Res. 2011, 50, 8859–8880

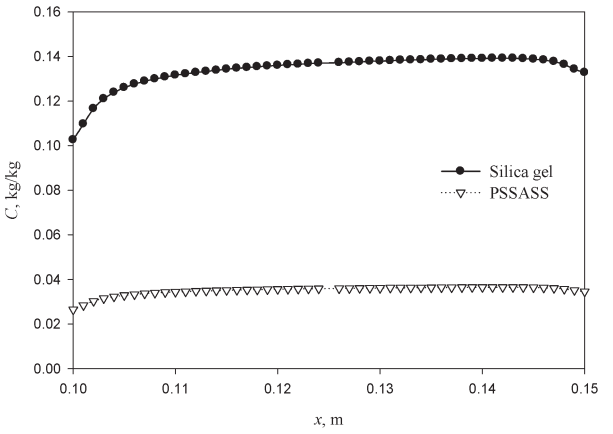

a. Desiccant surface concentration

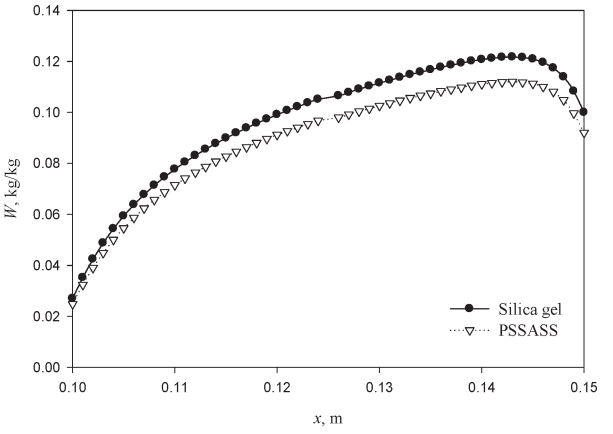

c. Desiccant surface water content

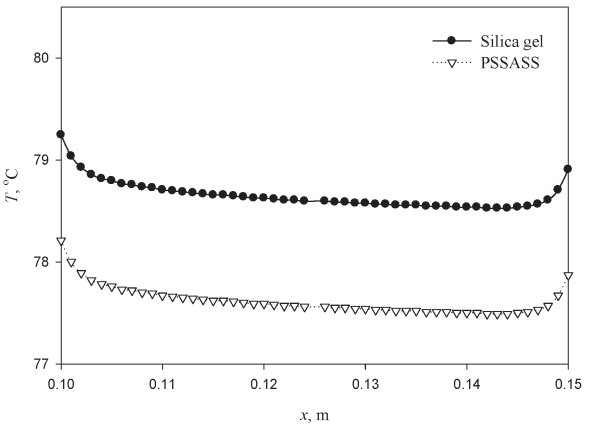

b. Desiccant surface temperature

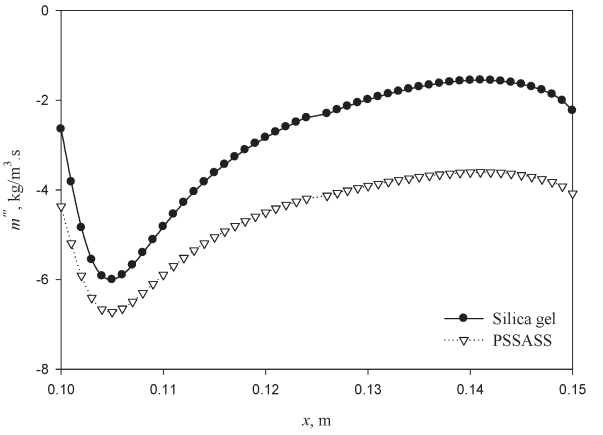

d. Desiccant surface water water desorption

Figure 24. Surface ($y = b$) (a) water concentration, (b) surface temperature, (c) overall average water content, and (d) overall average water desorption rate of model 2 for two different desiccants as a function of x. $u_\infty = 0.1$ m/s, $Re_L = 333$, $T_\infty = 30$ °C, $C_\infty = 0.015$ kg/kg, $C_b = 0.055$ (PSSASS) and 0.2 (silica gel) kg/kg, $W_0 = 0.135$ kg/kg, $L = 0.05$ m, $h = 0.05$ m, $b = 0.00321$ m, $\sigma = 0.5$, $d_p = 1.5 \times 10^{-3}$ m, $K = 0.71 \times 10^{-8}$, and $t = 4$ s.

AUTHOR INFORMATION

Corresponding Author

*E-mail: sharqawi@saudi.net.sa.

ACKNOWLEDGMENT

The authors are grateful to Professors Stuart W. Churchill and Howard Hu for their good counsel during the initial stages of this study.

NOMENCLATURE

b = thickness of silica gel bed, m
c = specific heat, kJ/(kg K)
c_{pa} = specific heat of air, kJ/(kg K)
c_{pv} = specific heat of vapor, kJ/(kg K)
C = water vapor concentration, (kg of water)/(kg of mixture)
C_E = Ergun constant
d_p = particle diameter, m
D = water vapor diffusivity in air, m^2/s
E_r = relative error
h = practical height in the y direction, m
h_m = convective mass-transfer coefficient, $kg/m^2 \cdot s$
h_1 = enthalpy of water vapor, kJ/kg
h_2 = enthalpy of air, kJ/kg
h_s = enthalpy in the solid desiccant, kJ/kg
H_l = adsorption heat, kJ/kg of water vapor
j = mass flux, $kg/m^2 \cdot s$
k = heat conductivity, $kW/(m \cdot K)$
K = permeability, m^2
L = length of the silica gel bed in the x direction, m
LE = leading edge
m'' = water mass flow rate (kg of water vapor)/$s \cdot m^2$
m''' = water absorption rate into silica gel, (kg of water vapor)/$s \cdot m^3$
p_r = relative pressure, Pa
Pr = Prandtl number
Re = Reynolds number
u = x component of velocity, m/s
Sh = Sherwood number
T = temperature, °C
t = time, s
TE = trailing edge
v = y component of velocity, m/s
W = water content, (kg of water vapor)/(kg of desiccant)

Greek Symbols

α = thermal diffusivity, m^2/s

ϕ = relative humidity in bulk stream, (kg of vapor)/(kg of air)
ν = kinematics viscosity, m^2/s
μ = viscosity, kg/m·s
ρ = density, kg/m^3
σ = porosity
Ω = slip velocity, m/s

Subscripts

ave = average
b = bed
e = effective
f = fluid (i.e., air)
s = solid desiccant
w = wall, i.e., the silica gel bed
∞ = free stream conditions

REFERENCES

(1) Al-Sharqawi, H.; Lior, N. Conjugate Computation of Transient Flow and Heat and Mass Transfer Between Humid Air and Desiccant plated and Channels. *Numer. Heat Transfer* **2004**, *46*, 525.

(2) Al-Sharqawi, H. S.; Lior, N. Effect of Flow-Duct Geometry on Solid Desiccant Dehumidification. *Ind. Eng. Chem. Res.* **2008**, *47*, 1569.

(3) Vafai, K.; Tien, C. L. Boundary and Inertia Effects on Flow and Heat Transfer in Porous Media. *Int. J. Heat Mass Transfer* **1981**, *24*, 195.

(4) Lee, K.; Howell, J. R. Theoretical and Experimental Heat and Mass Transfer in Highly Porous Media. *Int. J. Heat Mass Transfer* **1991**, *34* (8), 2123.

(5) Betchen, L.; Straatman, A. G.; Thomson, B. E. A Nonequilibrium Finite-Volume Model for Conjugate Fluid/Porous/Solid Domains. *Numer. Heat Transfer, Part A* **2006**, *49*, 543.

(6) Ergun, S. Fluid Flow Through Packed Column. *Chem. Eng. Prog.* **1952**, *48*, 89.

(7) Kaviany, M. *Heat transfer in porous media*; McGraw-Hill: New York,1998.

(8) Teng, H.; Zhao, T. S. An extension of Darcy's law to non-Stokes flow in porous media. *Chem. Eng.* **2000**, *55*, 2727.

(9) Combarnous, M. A.; Bories, S. A. Hydrothermal convection in saturated porous media. *Adv. Hydrosci.* **1975**, *10*, 231.

(10) Mei, V. C.; Lavan, Z. Performance of Cross-Cooled Desiccant Dehumidifiers. *ASME J. Solar Energy Eng.* **1983**, *105*, 300.

(11) Czanderna, A. W. Polymers as Advanced Materials for Desiccant Applications: 1. Commercially Available Polymers. *ASHRAE Trans.* **1989**, *95* (2), 1098.

(12) Beavers, S.; Joseph, D. D. Boundary conditions at a naturally permeable wall. *J. Fluid Mech.* **1967**, *30* (1), 197.

(13) Richardson, S. A model for the boundary condition of a porous material. Part 2. *J. Fluid Mech.* **1971**, *49* (1), 327.

(14) Taylor, G. L. A model for the boundary condition of a porous material. Part 1. *J. Fluid Mech.* **1971**, *49* (2), 319.

(15) Neale, G.; Nader, W. Practical Significance of Brinkman's Extension of Darcy's Law: Coupled Parallel Flows within a Channel and a bounding Porous Medium. *Can. J. Chem. Eng.* **1974**, *52*, 475.

(16) McQuiston, F. C.; Parker, J. D. *Heating, Ventilating, and Air Conditioning Analysis and Design*; Wiley: New York, 1994.

(17) Happel, J.; Brenner, H. *Low Reynolds Number Hydrodynamics*; Martinus Nijhoff Publishers: Dordrecht, The Netherlands, 1986.

(18) Carman, P. C. The Determination of the Specific Surface Area of Powder I. *J. Social Chem. Ind.* **1937**, *57*, 225.

(19) Reyes, S. C.; Iglesia, E. Monte Carlo Simulations of Structural Properties of Packed Beds. *Chem. Eng. Sci.* **1991**, *46* (4), 1089.

(20) Haughey, D. P.; Beveridge, G. S. G. Structural Properties of Packed Beds—A Review. *Can. J. Chem. Eng.* **1969**, *47*, 130.

(21) Al-Sharqawi, H. S. A Conjugate Transient Computational Analysis of Flow, Heat, and Mass Transfer in Desiccant-Airflow Systems. Ph.D. Dissertation, University of Pennsylvania, Philadelphia, PA, 2002.

(22) Ouchiyama, N.; Tanaka, T. Porosity of a Mass of Solid Particles Having a Range of Sizes. *Ind. Eng. Chem. Fundam.* **1981**, *20*, 66.

(23) Patankar, S. V. *Numerical Heat and Fluid Flow*; Taylor & Francis: New York, 1980.

(24) Pesaran, A. A.; Mills, A. F. Moisture Transport in Silica Gel Packed Beds—I, Theoretical Study. *Int. J. Heat Mass Transfer* **1987** *30* (6), 1037.

(25) Pesaran, A. A.; Mills, A. F. Moisture Transport in Silica Gel Packed Beds—II, Experimental Study. *Int. J. Heat Mass Transfer* **1987**, *30* (6), 1051.

(26) Nishioka, M.; Miyagi, T. Measurement of Distribution in the Laminar Wake of a Flat Plate. *J. Fluid Mech.* **1978**, *84*, 705.

(27) Caille, J.; Schetz, J. Finite-Element Navier−Stokes Analysis of the flow about a Finite Plate. *AIAA J.* **1989**, *27*, 1089.

(28) Collier, R. K.; Cale, T. S.; Lavan, Z. Advanced Desiccant Materials Assessment. AZ Final Report PB-87-172805/xab; Enerscop, Inc.: Glendale, CA, 1986.

(29) Pesaran, A. A.; Penney, T. R.; Czanderna, A. W. Desiccant Cooling: State of the Art Assessment. National Renewable Energy Laboratory Report NREL/TP; National Renewable Energy Laboratory: Golden, CO, 1992; p 254